ORIGINAL PAPER

Implications for metallogenic evolution of the giant Zhenyuan gold deposit (Yunnan, SW China) from textures and geochemical compositions of pyrite

Huichao Zhang[1,2] · Nigel J. Cook[3] · Hongrui Zhang[2] · Zengqian Hou[2] · Peng Chai[2] · Wei Li[4] · Sarah Gilbert[5]

Abstract

Pyrite, the most common sulfide mineral, is a ubiquitous component of many hydrothermal gold deposits. Geochemical patterns within the refractory pyrite structure represent a valuable repository of information that can help constrain the sources of ore-forming materials, and the evolution of ore-forming processes over time. However, there are still a lot of debates on the mechanisms of physico-chemical processes in ore-forming fluid controlling trace element and sulfur isotope distributions in pyrite during growth. In our manuscript, we use cutting-edge complementary microanalytical methods to understand the origin and evolution of zoned gold-bearing pyrite in samples from the largest gold deposit in the Ailaoshan gold belt, SW China, Zhenyuan (exceeding 100t Au, average grade: 5.3 g/t). Pyrite, arsenopyrite, chalcopyrite, and stibnite are the most abundant sulfide minerals in most orebodies. Of these, pyrite is dominant and is also the most important host for gold. Two types of pyrite can be clearly distinguished: framboidal pyrite and hydrothermal pyrite. Gold is most commonly hosted by hydrothermal pyrite. Framboidal pyrite, mainly hosted by carbonaceous slate, hosts negligible Au, and features low $\delta^{34}S$ values ranging from $-35.0\ (\pm 0.9)$ to $-25.6\ (\pm 1.0)$‰. Hydrothermal pyrite is characterized by complex intra-grain zoned textures with alternating As-rich and As-poor bands readily recognizable on backscattered electron images. Scanning electron microscopy and trace-element analyses show that both visible and invisible gold occur only in the As-rich bands. Compared to the As-poor bands (72.1% of Au concentration data < 1.96 ppm, $n = 43$), the As-rich bands are characterized by far higher concentrations of Au (up to 1420 ppm), Cu, Ag, Sb, and Tl, but lower concentrations of Co and Ni. *In-situ* sulfur isotope analysis indicates that the $\delta^{34}S$ values of As-rich zones range from $-7.3\ (\pm 0.6)$ to $2.9\ (\pm 0.6)$‰ and are similar to those of As-poor zones (from $-6.9\ (\pm 0.7)$ to $2.8\ (\pm 0.6)$‰), but distinct from the framboidal pyrite. Combined with published fluid inclusion data and a probable age for the magmatic event associated with mineralization, these data suggest that magmatic–hydrothermal fluids contributed most ore-forming materials and that periodic boiling led to formation of the rhythmic As-rich and As-poor bands in pyrite. Our data for pyrite constrain the evolution of ore-forming processes and provide new insights into the formation of zoned pyrite, with the conclusions having broad implications for analogous hydrothermal gold deposits worldwide.

Keywords Pyrite · Compositional zoning · Trace-element concentrations · NanoSIMS *in-situ* sulfur isotopes · Ailaoshan gold belt

---

Communicated by Daniela Rubatto.

✉ Hongrui Zhang
  zhanghr@yeah.net

✉ Zengqian Hou
  houzengqian@126.com

1   Institute of Marine Geology, College of Oceanography, Hohai University, Nanjing 210098, China

2   Institute of Geology, Chinese Academy of Geological Sciences, Beijing 100037, China

3   School of Chemical Engineering, The University of Adelaide, Adelaide, SA 5005, Australia

4   China University of Geosciences, Beijing 100083, China

5   Adelaide Microscopy, The University of Adelaide, Adelaide, SA 5005, Australia

Introduction

Pyrite is a major component of many hydrothermal gold deposits and can be a significant host for gold (Maddox et al. 1998; Williams-Jones et al. 2009; Velásquez et al. 2014; Zhang et al. 2022; Zheng et al. 2022). Previous studies suggest that textural relationships, compositions, and isotopic characteristics of pyrite can provide critical information on the sources of ore-forming materials and track the compositional evolution of hydrothermal systems (Large et al. 2009; Deditius et al. 2014; Tanner et al. 2016; Zhang and Zhu 2016, 2017; LaFlamme et al. 2018a; Li et al. 2020a). Several recent publications have emphasized that changes in texture, trace-element endowment, and sulfur isotopic composition of pyrite reflect variation of physico-chemical conditions (such as temperature, pressure, and pH) of ore-forming fluids (Tardani et al. 2017; Li et al. 2021a; Sugiono et al. 2022). The ratios among certain trace elements and the sulfur isotope signatures of pyrite have been proposed as tools to discriminate the evolution of physico-chemical conditions (Román et al. 2019; Keith et al. 2022). Nevertheless, the mechanisms by which physico-chemical processes control trace element and sulfur isotope distributions in pyrite during growth, and how these phenomena are preserved in an evolving system, require additional research.

Individual pyrite crystals can contain a range of different texture and compositions, expressed as zoned textures. These pyrites are thus ideal materials to link chemistry and preserved textures to physico-chemical conditions and fluid processes. Each pyrite grain with zoned texture represents a time-resolved record of the complex processes during precipitation and growth (e.g.,Cook et al. 2009; Reich et al. 2013). Many mechanisms have been suggested to explain the origin of zoned pyrite, including kinetic effects during crystallization, such as growth rate and diffusion-limited self-organization processes, and changes in fluid chemical composition caused by fluid–rock reactions, mixing, and boiling (Deditius et al. 2009; Fougerouse et al. 2016; Tardani et al. 2017; Li et al. 2018; Wu et al. 2019). These mechanisms are recorded and readily identified by textures, patterns of trace-element distribution, and by measurable variation in isotope compositions across discrete zones (Román et al. 2019).

The Ailaoshan gold belt is the most economically important part of the Sanjiang Tethyan metallogenic domain (Hou et al. 2007; Zhang and Hou 2015). It hosts four large gold deposits, among which Zhenyuan is the largest (Zhang et al. 2014a; Deng et al. 2015; Wang et al. 2016). Previous research indicates that both magmatism and faulting leading to shearing operated during periods of mineralization (Zhang et al. 2012; Liu et al. 2015; Li et al.

2019a, b; Wang et al. 2020). In the Zhenyuan gold deposit, hydrothermal pyrites generally show alternating As-rich and As-poor zones, which have distinct textural and compositional characteristics. Zhenyuan pyrite, therefore, represents an exemplary study case to relate the textural and compositional record with evolution in physico-chemical conditions, ongoing magmatism, faulting, and other geological processes.

In this study, we have addressed the complexity and evolution of the pyrite from Zhenyuan in a systematic investigation of micro-to-nanoscale textures, coupled with in-situ determination of major, trace element, and sulfur isotopic characteristics. This major deposit, with its spectacularly zoned pyrite represents an ideal case to test and refine hypotheses regarding formation of zoned pyrite, with implications for analogous hydrothermal gold deposits worldwide.

Regional and deposit geology

The Ailaoshan tectonic belt, located within the southeastern part of the Sanjiang Tethyan Orogen, tectonically connects the Yangtze–South China block to the east and the Indochina block to the west (Fig. 1a, b; Hou et al. 2007; Deng et al. 2010; Liu et al. 2015; Wang et al. 2016; Xiao et al. 2017; Xu et al. 2021). It comprises several regional fault zones, from northeast to southwest, these are the Red River fault, Ailaoshan fault, and Jiujia–Anding fault. All three strike nearly NW and dip to NE at 60–80°. The Ailaoshan tectonic belt is divided by the Ailaoshan fault into the Proterozoic Ailaoshan Group in the east, and the Paleozoic–Mesozoic unit in the west (Fig. 1b). The Ailaoshan Group mostly consists of lower amphibolite to granulite facies metamorphic rocks, and the Paleozoic–Mesozoic unit is composed of rocks that have undergone regional metamorphism only up to greenschist facies (Liu et al. 2015). The Ailaoshan suture zone, located between the high-grade metamorphosed unit and the low metamorphosed grade unit, formed via Late Permian closure of the Ailaoshan branch of Paleo-Tethyan Ocean (Zhong 1998; Deng et al. 2015).

Cenozoic high-potassium alkaline rocks with ages ranging between 41 and 32 Ma, and 28–23 Ma calc–alkaline magmatic rocks outcrop widely across the Ailaoshan tectonic belt (Liang et al. 2007; Liu et al. 2015). Cenozoic lamprophyres with phlogopite Ar–Ar ages of 29.6–36.8 Ma, should also be noted (Chen et al. 2014). In addition, Late Proterozoic and Late Permian–Triassic magmatic rocks have been reported in this belt (Qi et al. 2010; Zhang et al. 2011; Wang et al. 2012, 2020; Liu et al. 2013, 2014).

The Ailaoshan gold belt is the region between the Jiujia–Anding and Ailaoshan faults, and consists of unmetamorphosed or up to greenschist facies metamorphic Paleozoic–Mesozoic units. The belt hosts numerous gold
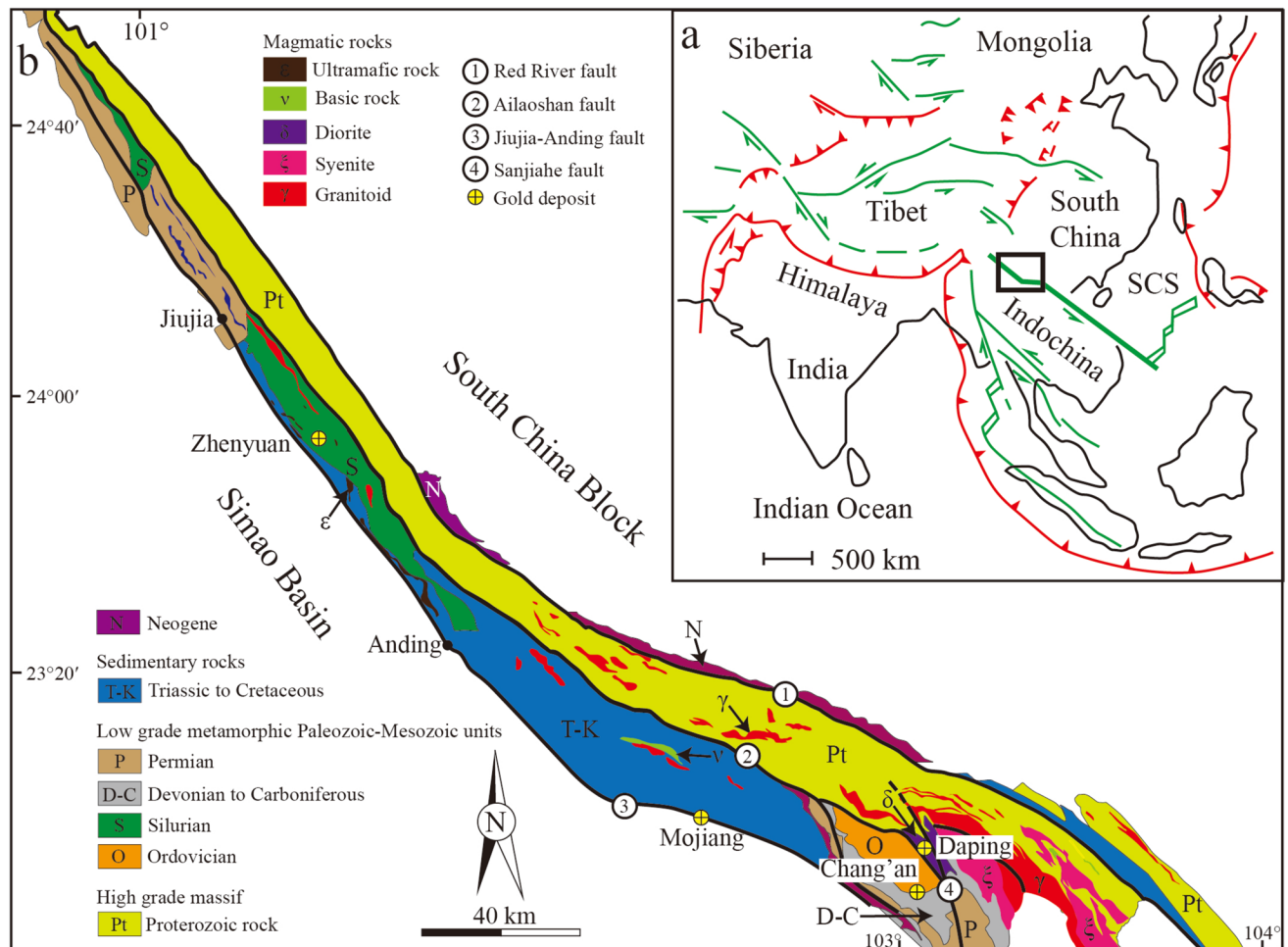
Fig. 1 a Simplified geological map showing the Indian–Eurasian collision zone. **b** Tectonic map of the Ailaoshan gold belt, SW China. Locations of the Cenozoic gold deposits are indicated. Modified from Deng et al. (2015) and Liu et al. (2015)

deposits, including Zhenyuan (> 100 t Au), Mojiang (> 30 t Au), Chang'an (> 30 t Au), and Daping (> 60 t Au) (Ge et al. 2007; Sun et al. 2009; Yang et al. 2010, 2021; Deng et al. 2010; Li et al. 2019a). Zhenyuan, in the northern part of the belt, is by far the largest deposit among these, with a current resource (measured and indicated) exceeding 100 t Au at an average grade of 5.3 g/t (Shi et al. 2012; Li et al. 2020b; Wang et al. 2022). The two largest deposit orebody clusters making up the deposit are Laowangzhai (4.16 Mt @ 5.29 g/t Au) and Donggualin (8.82 Mt @ 5.10 g/t Au) (Supplemental Fig. S1; Yang et al. 2010). The strata exposed in the Zhenyuan deposit are mostly the Upper Devonian Kudumu, Lower Carboniferous Suoshan, and Upper Triassic Yiwanshui Formations (Supplemental Fig. S1). Ultramafic–mafic rocks, in faulted contact with the aforementioned metasedimentary rocks, include olivine pyroxenite, harzburgite, and basalt (Ren et al. 1995). Late Permian felsic intrusions (zircon U–Pb ages 255–247 Ma) intrude both the metasedimentary units and ultramafic–mafic

rocks (Li et al. 2013a). Lamprophyre dikes with phlogopite $^{40}Ar–^{39}Ar$ ages of 34–31 Ma are also widely exposed in the Laowangzhai and Donggualin mines (Wang et al. 2001; Gan and Huang 2017).

The Laowangzhai orefield is controlled by NW and NE-striking faults. The main orebody clusters seen in the Laowangzhai mine (labeled as III, IV, and V on Supplemental Fig. S1) are strictly controlled by the F14, F19, and F7 faults, respectively (Zhang et al. 2012). In the open pit of Laowangzhai mine (orebody cluster V), the main exposed rocks are Early Carboniferous carbonaceous slate and quartz sandstone, which are intruded by Late Permian quartz porphyry and Eocene lamprophyre (Fig. 2a). Orebodies are generally located at the contacts between quartz porphyry, carbonaceous slate, and quartz sandstone (Fig. 2a–d). Representative ore samples from the open pit and underground mining areas of orebodies III, IV, and V were investigated (see sample locations and types in Supplemental Figs. S2a and S3). These samples cover mineralized quartz porphyry (Fig. 2c),
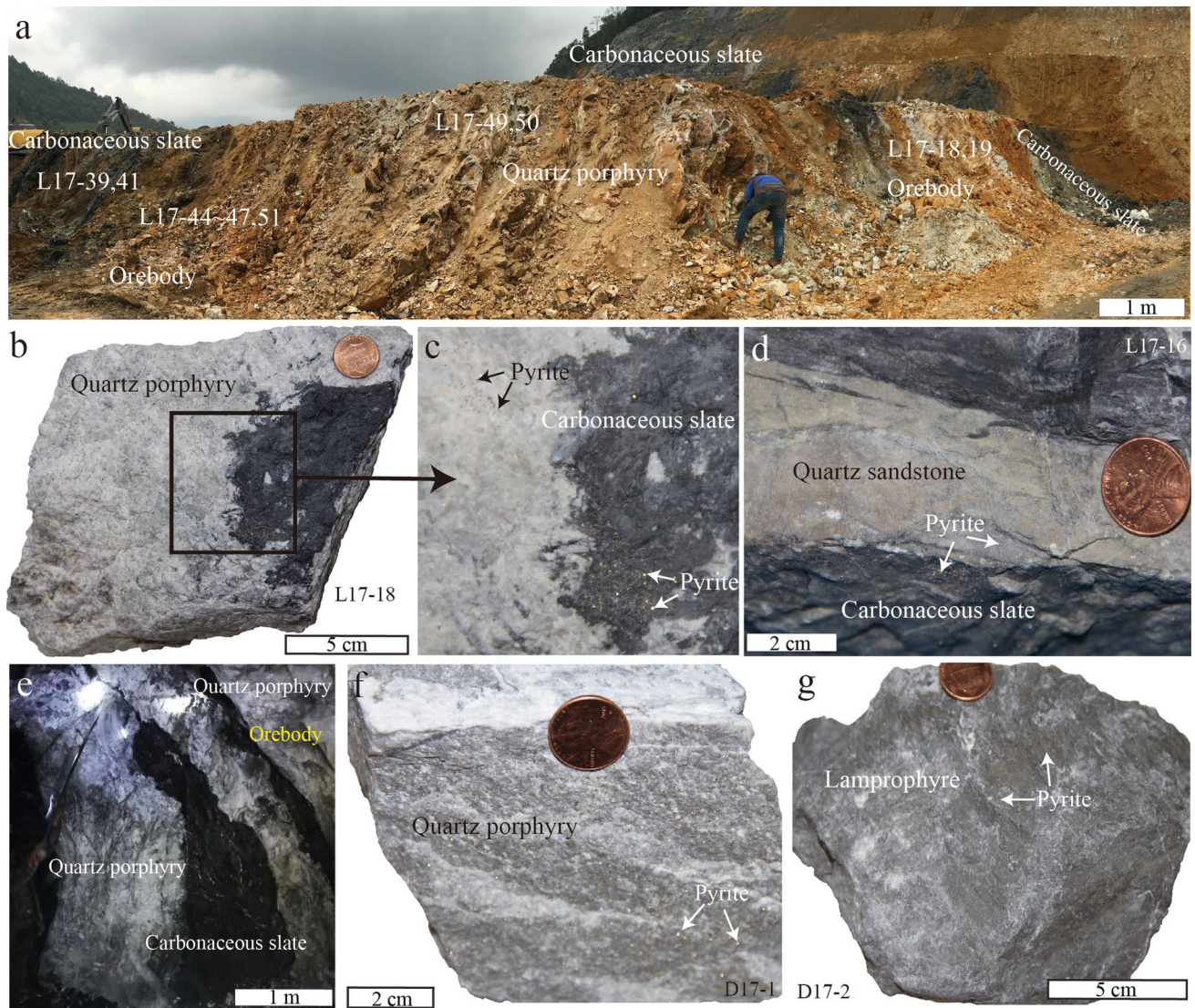
Fig. 2 Occurrence of orebodies and ore samples in the Zhenyuan gold deposit. **a** Open pit mining area in Laowangzhai mine with orebodies located between the quartz porphyry and carbonaceous slate; **b, c** pyrite generally occurs in the contact zone between the quartz porphyry and carbonaceous slate; **d** pyrite in the contact zone between the quartz sandstone and carbonaceous slate; **e** samples from the orebody hosted by quartz porphyry in Donggualin mine; **f** quartz porphyry ores with disseminated pyrites; **g** lamprophyre-hosted ores with disseminated pyrites

carbonaceous slate, and quartz sandstone (Fig. 2d), and contain disseminated pyrite and minor quartz–pyrite veinlets (Supplemental Fig. S3). Three main orebody clusters (SI, SII, SIII) are identified in the Donggualin mine (Supplemental Fig. S1), in which NW-striking faults control the distribution and occurrence of orebody clusters. Ores hosted by quartz porphyry (1543 m level, Fig. 2e, f), lamprophyre (1563 m level, Fig. 2g), and carbonaceous slate (1753 m and 1673 m level) from orebody SI, SII, and SIII were sampled (see sample locations and types in Supplemental Figs. S2b and S4). These ores all contain abundant finely disseminated pyrite.

Analytical methods

Ore textures, pyrite major and trace element, and sulfur isotope compositions were analyzed in this study. The scanning electron microscope (SEM) used (FEI Quanta 650 FEG, Peking University) is equipped with an energy-dispersive spectrometer (EDS), allowing backscattered electron (BSE) imaging of mineral morphologies and qualitative compositional data.

To investigate the physical form of gold in Au-rich pyrite, solid solution or nanoparticles, transmission electron microscopy (TEM) analysis was conducted. Fragments from As- and Au-rich pyrite for TEM analysis were extracted

in-situ using the focused ion beam (FIB) technique at the Institute of Geology and Geophysics, Chinese Academy of Sciences (IGG–CAS). The FIB cutting was conducted with a Zeiss Auriga Compact dual beam instrument equipped with an Omniprobe AutoProbe 200 micromanipulator. Ion beam conditions for the final thinning and polishing were 5–30 kV with beam currents of 50 pA to 2 nA. The FIB section was thinned to ~ 100 nm. Bright-field (BF) imaging was performed using a JEOL JEM-2100 microscope operated at 200 kV, and with the electron beam generated from a LaB6 gun. Chemical compositions were acquired using the built-in Oxford X-max 80 energy-dispersive X-ray spectrometer (EDXS). Details of TEM methodologies are given by Tang et al. (2023).

Quantitative compositional data (Supplemental Table S1) were obtained using a JEOL JXA-8230 electron probe microanalyser (EPMA) at the Chinese Academy of Geological Sciences, Beijing. Elements and X-ray lines used were Fe (Kα), As (Lα), S (Kα), Pb (Mα), Ni (Kα), Ag (Lα), Cu (Kα), Zn (Kα), Co (Kα), Sb (Lα), and Au (Lα). For sulfide minerals, operating conditions were an accelerating voltage of 20 kV, beam current of 10 nA, and an electron beam approximately 1 µm in diameter. Count times were 10 s on peak, 5 s on low background position and 5 s on high background position for each element. Natural and synthetic mineral standards of chalcopyrite, pyrite, sphalerite, galena, CoNiAs, and native silver, antimony and gold were used for calibration. The ZAF correction method, consisting of atomic number correction (Z), absorption correction (A), and fluorescence correction (F), was applied for standardization. Average minimum detection limits (mdl) of elements in sulfide minerals are as follows (in ppm): Fe (176), As (232), S (71), Ni (152), Co (153), Pb (413), Sb (131), Zn (184), Cu (160), Ag (119), and Au (146).

Each sample for trace element analysis and element mapping of sulfide minerals was prepared as a 1-inch-diameter polished block. These polished blocks were analyzed using a 213 nm, Q-switched, Nd: YAG NWR213 laser ablation system (Elemental Lasers), coupled to an Agilent 7900 Quadrupole ICP–MS instrument (Adelaide Microscopy, University of Adelaide, Australia). LA–ICP–MS analysis of pyrite was performed in spot mode using a laser beam diameter of 10 to 25 µm, a repetition rate of 5 Hz, and laser energy of 4.0 to 5.5 J/cm^2. Total acquisition time for each analysis was 70 s (30 s background measurement followed by 40 s of sample ablation). Calibration for LA–ICP–MS spot analysis was performed using USGS sulfide reference material MASS-1 (Wilson et al. 2002). Monitored isotopes included ^{34}S, ^{55}Mn, ^{57}Fe, ^{59}Co, ^{60}Ni, ^{63}Cu, ^{66}Zn, ^{69}Ga, ^{75}As, ^{77}Se, ^{95}Mo, ^{107}Ag, ^{111}Cd, ^{115}In, ^{118}Sn, ^{121}Sb, ^{125}Te, ^{197}Au, ^{201}Hg, ^{205}Tl, ^{208}Pb, and ^{209}Bi. ^{57}Fe served for internal calibration, using measured wt.% data from EPMA of the same or similar grain. ^{115}In was corrected for isobaric interference from ^{115}Sn using the measured ^{118}Sn and assuming natural isotopic abundance. Minimum detection limits depend on spot size, which governs ablated mineral volume. Average minimum detection limits for trace elements in pyrite (in ppm) are Co (0.28 ± 0.17), Ni (1.43 ± 0.82), Cu (5.76 ± 3.84), As (11.83 ± 5.82), Ag (1.33 ± 0.72), Sb (0.43 ± 0.22), Au (0.31 ± 0.62), Tl (0.11 ± 0.05), Pb (0.61 ± 0.49), and Bi (0.15 ± 0.07) (Supplemental Table S2).

LA–ICP–MS mapping of pyrite was conducted by ablating sets of parallel lines scanned across an area of the sample using beam sizes ranging from 8 to 15 µm depending on grain size, at a laser frequency of 10 Hz. The speed of the line scans was the same as the spot size used (e.g., 8 µm/s for an 8 µm beam size). Re-deposition during mapping was minimized by pre-ablating each line prior to data collection. Identical raster lines were made on the MASS-1 reference material at the start and end of each mapping run to correct for instrument drift. All data reduction was performed using Iolite, an open-source software package for processing ICP–MS data, as an add-in for the data analysis program Igor developed by WaveMetrics (Paton et al. 2011).

Sulfur isotope analysis of pyrite was performed using a Cameca nanoscale secondary ion mass spectrometry (NanoSIMS) 50L at IGG–CAS. Samples were polished and carbon-coated for conductivity at high voltage. A Cs$^+$ beam current of ~7–10 pA with a diameter of 250 nm was rastered across the sample surface. Before image acquisition, the selected area was sputtered with a high intensity beam of 1 nA for 2 min to remove the coating and to implant enough Cs$^+$ into the sample surface to stabilize the yield of the secondary ions. Areas 2×2 µm in size were selected for spot analyses of the ^{34}S/^{32}S ratio each time with an electron multiplier for the ^{34}S$^-$ signal and a Faraday cup for the ^{32}S$^-$. The standard material (PY-1117) was used to correct for instrumental mass fractionation. The reproducibility of δ^{34}S measurements on the PY-1117 pyrite is 0.55‰ during the analytical session (Supplemental Table S3). The uncertainty on single spot analyses (SE$_{sample}$) were estimated by the following formula (Hao et al. 2023):

$$SE_{sample} = \sqrt{SE_{Spot}{}^2 + SD_{standard}{}^2 + SD_{ref.}{}^2}$$

SE$_{sample}$ is estimated as the square sum of the reproducibility of δ^{34}S measurements on the corresponding pyrite standard of PY-1117 (SD$_{standard}$), the internal precision of each spot on the sample (SE$_{spot}$) and the uncertainty of the reference values of the PY-1117 standard (SD$_{ref.}$), which are determined by stable isotope mass spectrometry with δ^{34}S$_{V-CDT}$ value of 0.3 ± 0.1‰, which can be found in Zhang et al. (2014b) and Hao et al. (2023). Detailed analytical conditions are identical to those described by Zhang et al. (2014b).

Results

Textural characterization of pyrite

Orebodies with different host rocks from the Laowang-zhai and Donggualin mines all share similar sulfide assemblages that include pyrite, arsenopyrite, chalcopyrite, and stibnite. Pyrite, the most abundant sulfide, can be broadly subdivided into framboidal pyrite and hydrothermal pyrite. Framboidal pyrite occurs only in the carboniferous slate, where it displays a texture of microscopic spheroidal to sub-spheroidal pyrite clusters ranging from 5 to 60 μm in size. Framboidal pyrite is preferentially concentrated in black bands where it coexists with irregular carbonaceous material oriented nearly parallel to bedding (Fig. 3a, b). Framboidal pyrite may also occur as inclusions within carbonaceous material (Fig. 3c, d). Spheroidal framboids commonly consist of cubic microcrystals of pyrite cemented by later pyrite (Fig. 3e, f). Hydrothermal pyrite commonly encloses framboidal pyrite, inferring formation of framboidal pyrite prior to hydrothermal activity.

Hydrothermal pyrite in ores, including disseminated sulfide minerals and quartz–pyrite veinlets, hosted by different host rocks from Laowangzhai and Donggualin mines, commonly displays euhedral to subhedral morphology, and diameters ranging from 50 to 400 μm. It generally shows complex internal structure, with a yellow core in reflected light enclosed by a recognizably pink overgrowth. This overgrowth is, in turn, surrounded by a further yellow overgrowth, and finally rimmed by an idiomorphic pink overgrowth (Fig. 4a). These intricate zoned textures can be clearly recognized as alternating dark and bright zones on BSE images (Fig. 4b). The dark zone corresponds to As-poor pyrite, whereas the bright zone is As-rich. The As-poor zone is usually corroded by the As-rich overgrowth (Fig. 4b, c, f). Arsenopyrite, mostly represented by euhedral to subhedral crystals, only occurs as inclusions within As-rich pyrite (Fig. 4b, c), but may also form an overgrowth on the whole pyrite (Fig. 4d). Occasionally, pyrite is overgrown by arsenopyrite, which is, in turn, surrounded by another pyrite overgrowth (Fig. 4e). Similarly, stibnite and chalcostibite only occur as inclusions in As-rich zones of pyrite (Fig. 4c, g). Relative to the As-rich zone, the As-poor zone of pyrite contains more inclusions of quartz and monazite (Fig. 4f). Previous research at Zhenyuan did not observe much native gold, leading researchers to consider that most Au was invisible or refractory in nature. Our higher magnification imaging, however, enabled identification of sub-micron grains of native gold within the As-rich zone of pyrite (Fig. 4h). It is noteworthy that several disseminated pyrite grains are surrounded by pressure shadows filled with oriented quartz

(Fig. 4i). Disseminated sulfide minerals and quartz–pyrite veinlets are crosscut by later calcite–quartz–stibnite–pyrite veinlets, in which pyrite shows no zoned texture and no micro-inclusions of gold were observed.

Pyrite major and trace-element composition

Major element compositional datasets for pyrite (Supplemental Table S1) reveal that framboidal pyrite from the carboniferous slate is generally poor in As (< 0.11 wt.%), Ni (< 0.07 wt.%), and Co (0.07–0.13 wt.%). No other trace or minor components are present at concentrations measurable by EPMA. Trace-element concentration data for framboidal pyrite were obtained by LA–ICP–MS. Time-resolved LA–ICP–MS depth profiles were checked and display reasonably smooth signals across the integrated count range for most elements (Supplemental Fig. S5). All depth profiles with obvious peak signals indicative of inclusions were not processed further. Trace-element data for framboidal pyrite are summarized in Supplemental Table S2. Framboidal pyrite from carboniferous slate contains limited concentrations of Co (Median value 28.7 ppm), Ni (171 ppm), Ag (5.15 ppm), Cu (46.4 ppm), As (174 ppm), Sb (27.0 ppm), Tl (0.28 ppm), Pb (85.6 ppm), and Bi (0.62 ppm). Concentrations of Au are generally < mdl.

Most hydrothermal pyrite grains in ores from the Laowangzhai and Donggualin mines hosted by different types of wall-rocks share similar compositional characteristics. The As contents of hydrothermal pyrite with zoned textures vary significantly, consistent with the different colors visible under the microscope and strong brightness variation on BSE images (Fig. 4a, b). EPMA data indicate pyrite cores are commonly As-poor (< 1.56 wt.%), whereas the overgrowths contain far higher As (7.61 to 14.63 wt.%; Fig. 5a, b; Supplemental Table S1). A zone between the As-rich and As-poor zones contains intermediate As contents (1.95 to 6.38 wt.%; Fig. 5b-–d; Supplemental Table S1). The negative correlation between As and S (Fig. 5c) suggests that As is likely incorporated by substitution for S (Palenik et al. 2004; Deditius et al. 2008). Substitution of S by As can also be verified by EDS mapping, which shows the bright zone in BSE images is rich in As and relatively poor in S (Fig. 6a–c). Arsenic-poor and As-rich zones both contain measurable Co and Ni, but the As-poor zone contains more Co and Ni than the As-rich zone (Fig. 5d). In contrast, the Fe contents of the two zones are similar (Fig. 6d), suggesting that Fe does not participate in the substitution. To better understand the occurrence of Au, a fragment of an As-rich zone in pyrite was extracted for TEM analysis using the FIB extraction-lifting technique (Fig. 6a, e). TEM imaging revealed several nanoscale grains of chalcopyrite and stibnite within the
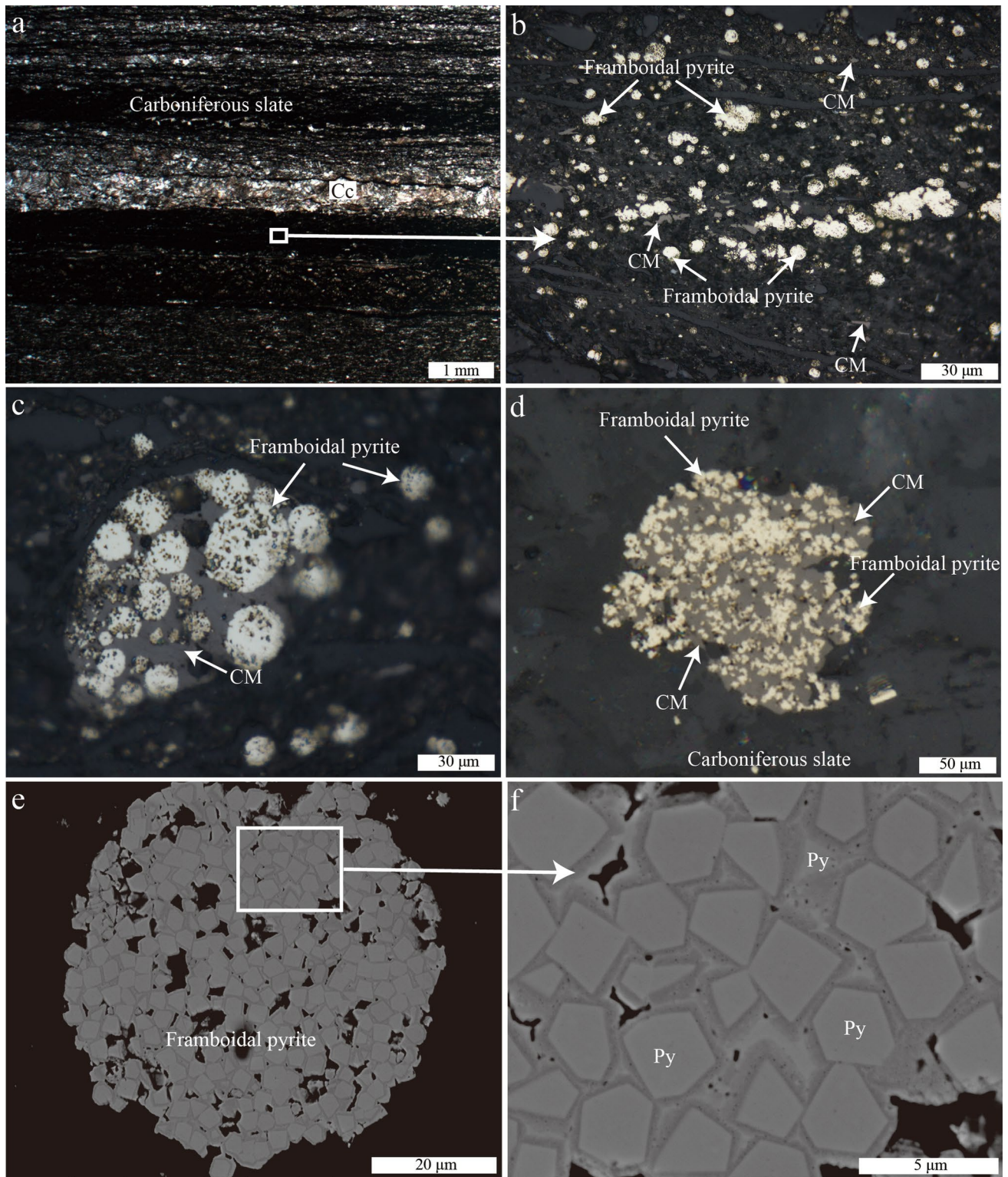
Fig. 3 Photomicrographs of framboidal pyrites from carbonaceous slate. **a**, **b** Framboidal pyrite is preferentially concentrated in black bands; **c** framboidal pyrite coexists with irregular carbonaceous material; **d** framboidal pyrites occur in the carbonaceous material as inclusions; **e**, **f** framboidal pyrite commonly consists of microcrystals of pyrite, which were cemented by later pyrites. Mineral abbreviations: *CM* carbonaceous material, *Py* pyrite
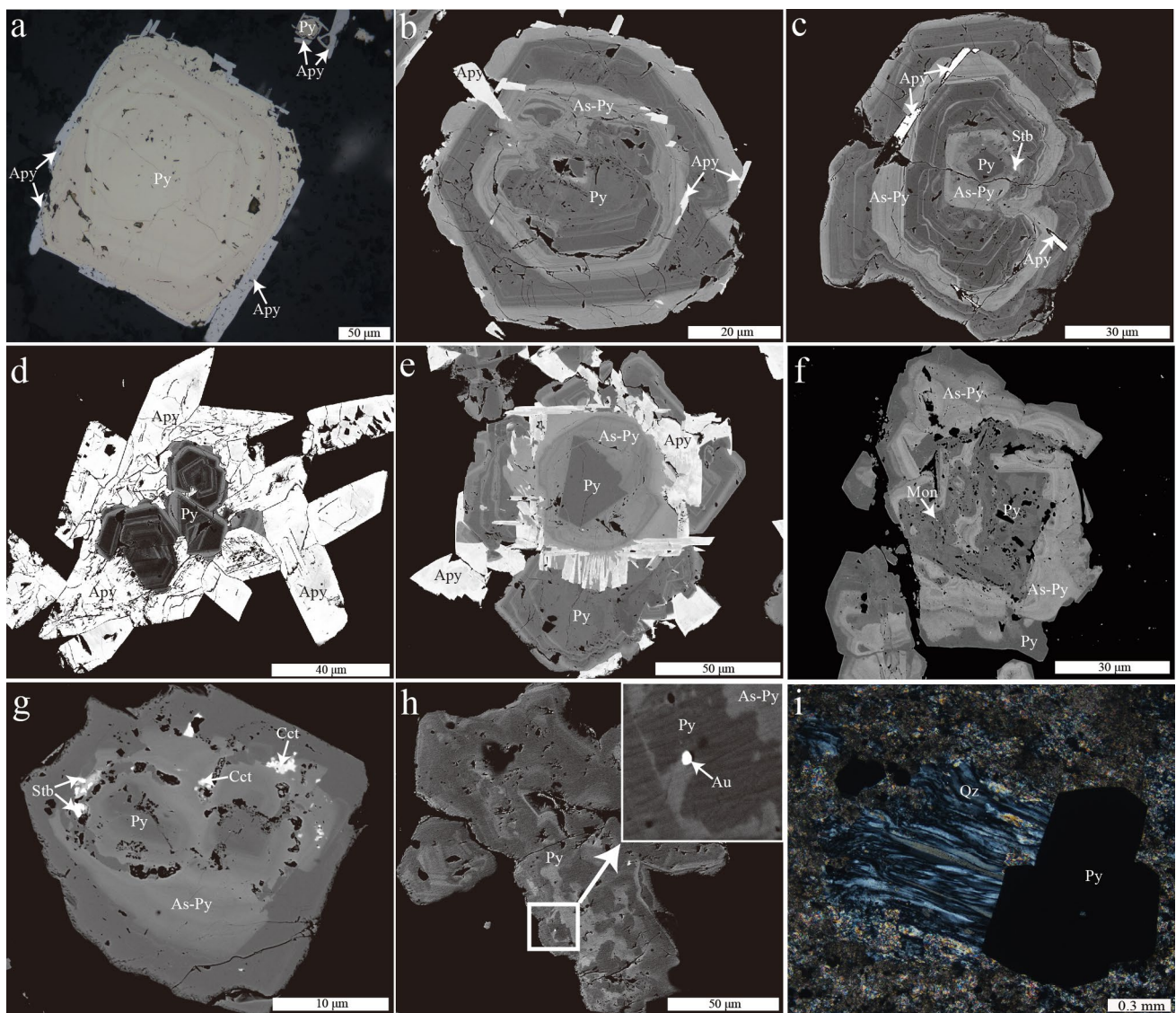
Fig. 4 Photomicrographs of hydrothermal pyrites with zoned texture. **a** Pyrite displays complex internal texture and is enclosed by arsenopyrite (reflected light); **b** alternating As-rich and As-poor bands in pyrite hosted by quartz porphyry (BSE); **c** arsenopyrite and stibnite only occur in the As-rich zone of pyrite (BSE); **d** pyrite with zoned texture enclosed by arsenopyrite (BSE); **e** As-rich zones of pyrite coexist with arsenopyrite (BSE); **f** zoned pyrite hosted by lampro- phyre (BSE); **g** chalcostibite also only occurs in the As-rich zone of pyrite hosted by lamprophyre (BSE); **h** sub-micron grains of native gold within the As-rich zone of pyrite (BSE); **i** pyrite grain sur- rounded by pressure shadows filled with oriented quartz. Mineral abbreviations: *As-Py* As-rich pyrite, *Apy* arsenopyrite, *Au* native gold, *Cct* chalcostibite, *Mon* monazite, *Py* pyrite, *Qz* quartz, *Stb* stibnite

bright zone, but no nanoscale grains of native gold or other Au-bearing phases could be identified (Fig. 6f, g).

LA–ICP–MS trace-element mapping was conducted on zoned hydrothermal pyrite. Results reveal that the As-rich and As-poor zones in pyrite contain distinct trace-element contents (Fig. 7; Supplemental Fig. S6). In general, the inner and outermost As-rich zones are the richest in both Au and Cu (Fig. 7b–d). Antimony, Tl, and Ag are prefer- entially enriched at the outermost As-rich zones, whereas the inner As-rich zones contain these elements at concen- trations comparable with the As-poor zones (Fig. 7e, g).

In addition, Ni distributions commonly resemble those of Co and that these two elements are concentrated in As- poor zones (Fig. 7h, i). Several pyrite grains show dark As-poor cores, bright As-rich mantles, and dark As-poor rims on BSE images (Fig. 8a). In the center of an As-poor core, an area is replaced by later fluid along the fracture (Fig. 8a); therefore, the composition of this area cannot represent the composition of As-poor core. Apart from this area, our mapping shows that the As-rich mantles are commonly enriched in Cu, Au, Ag, Sb, and Tl relative to the cores (Fig. 8b–g). These As-rich mantles can be further
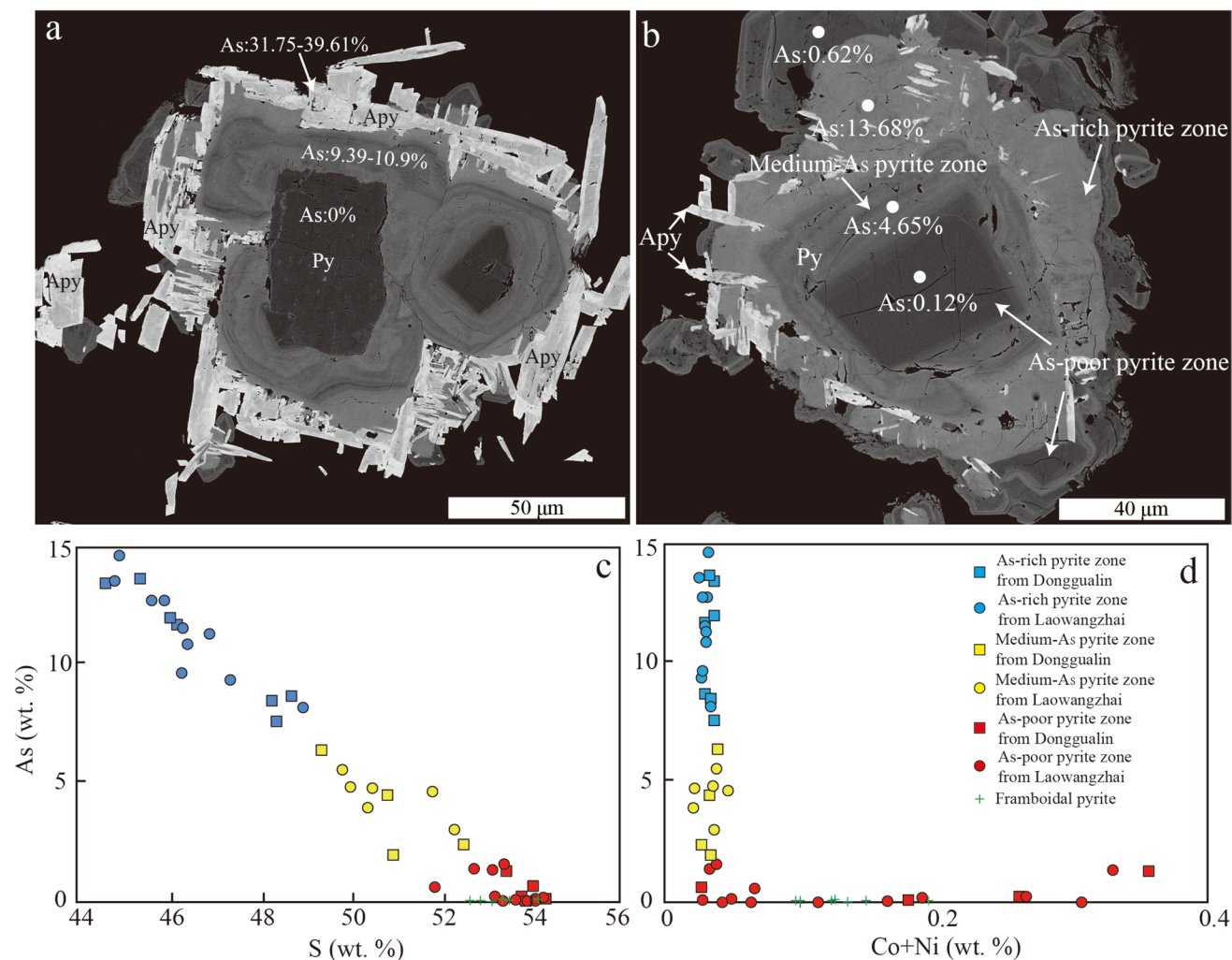
Fig. 5 Chemical compositions of representative framboidal and hydrothermal pyrite (EPMA data). **a** Hydrothermal pyrite and arsenopyrite with As contents on corresponding zones (Laowangzhai mine, BSE); **b** hydrothermal pyrite with As contents on corresponding zones (Donggualin mine, BSE); **c** As vs. S variation in framboidal and hydrothermal pyrite; **d** As vs. Co + Ni variation in framboidal and hydrothermal pyrite. Mineral abbreviations: *Apy* arsenopyrite, *Py* pyrite

divided into two parts: an inner mantle and an outer mantle, separated from one another by a thin As-poor band (Fig. 8a). Arsenopyrite only occurs in the As-rich outer mantle, which has higher As concentrations than the inner mantle (Fig. 8a). In contrast, Co and Ni display marked enrichment in the As-poor core, whereas the mantles contain almost no Co or Ni (Fig. 8h, i).

Quantitative trace-element concentration data for hydrothermal pyrite were obtained by LA–ICP–MS in spot analysis mode. Trace-element data are summarized in Supplemental Table S2. As a whole, hydrothermal pyrite from ores hosted by quartz porphyry, lamprophyre, quartz sandstone, and carbonaceous slate, all have similar trace-element concentrations including Au. Our spot analyses verify the results from mapping that the As-poor zones

and As-rich zones of pyrite have distinctly different trace-element concentrations (Fig. 9).

Arsenic-poor zones (< 15,000 ppm) contain only a small amount of Au with most data < 1.96 ppm (72.1%, $n = 43$), whereas Au concentrations can attain up to as much as 1420 ppm in the As-rich zones and most data are > 1.91 ppm (65.0%, $n = 80$) (Fig. 9a; Supplemental Table S2). Copper concentrations in As-rich zones range over several orders of magnitude from < mdl to 2080 ppm with most values > 100 ppm (78.8%, $n = 80$), but the As-poor zones of pyrites usually contain lesser Cu with most values < 100 ppm (74.4%, $n = 43$; Fig. 9b; Supplemental Table S2). Silver concentrations can reach up to as much as 46.1 ppm with most values > 1 ppm (57.5%, $n = 80$) in As-rich zones (Supplemental Table S2), whereas the Ag
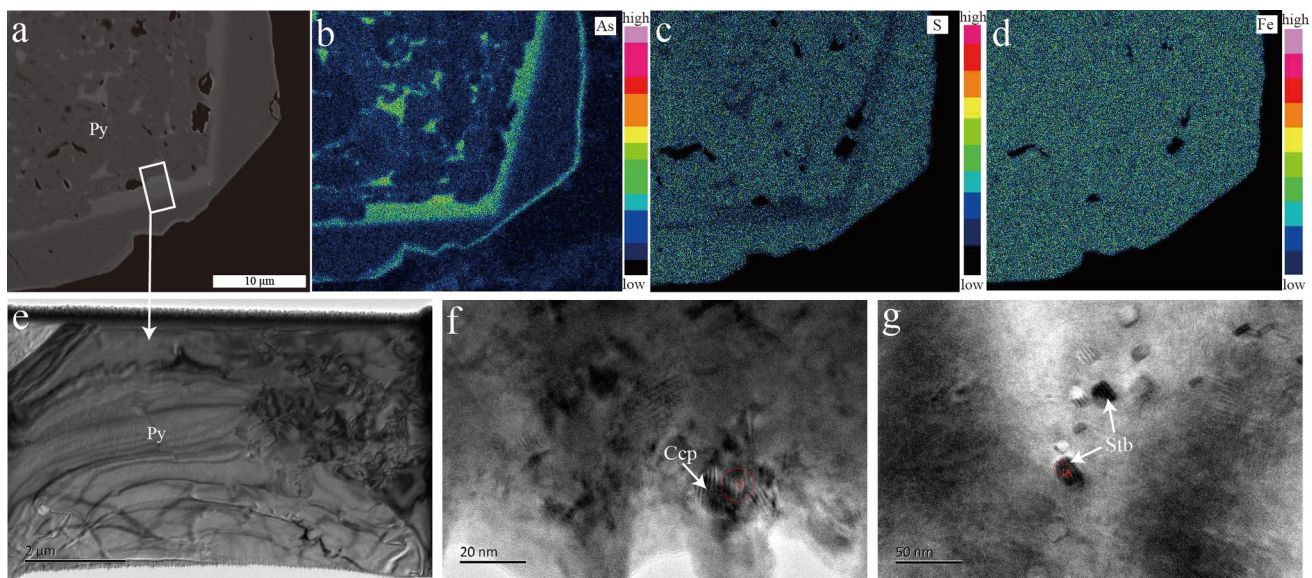
Fig. 6 EDS maps and TEM photomicrographs of hydrothermal pyrite. **a** Hydrothermal pyrite with zoned texture, BSE; **b**, **c** bright zone is richer in As and poorer in S than the dark zone; **d** iron is evenly distributed across both zones; **e** Sample extracted from the bright zone using FIB technique for TEM analysis, bright-field image; **f**, **g** sub-micron chalcopyrite and stibnite grains were identified under the TEM, bright-field image. Mineral abbreviations: *Py* pyrite, *Ccp* chalcopyrite, *Stb* stibnite

concentrations in As-poor zones are commonly < 1 ppm (62.8%, $n = 43$). Concentrations of Tl and Sb generally display a positive correlation with As (Fig. 9c). The Tl and Sb concentrations in As-rich zones range from 0.14 to 39.0 ppm ($n = 80$) and from 13.5 to 1900 ppm ($n = 80$), respectively (Fig. 9c, Supplemental Fig. S6g; Supplemental Table S2). However, the Tl and Sb concentrations in As-poor zones range from < mdl to 7.05 ppm ($n = 43$) and from 0.45 to 397 ppm ($n = 43$), respectively. A similar relationship is observed between Co and Ni (Fig. 9d). Like the mapping, trace-element spot analysis shows that Co and Ni have distribution trends that are distinct from other elements. Cobalt concentrations in the As-poor zones of pyrite range from < mdl to 1940 ppm with most data > 116 ppm (55.8%, $n = 43$) and Ni concentrations range from < mdl to 2850 ppm with most data > 108 ppm (70.0%, $n = 43$). The Co and Ni concentrations in As-rich zones vary from < mdl to 1940 ppm (with most data < 116 ppm, 88.8%, $n = 80$) and from < mdl to 1460 ppm (with most data < 108 ppm, 66.2%, $n = 80$), respectively (Supplemental Table S2). In general, the As-rich zones of hydrothermal pyrite appear relatively enriched in Au, Cu, Ag, Sb, and Tl, whereas Co and Ni are preferentially concentrated in the As-poor zones.

Sulfur isotope analysis

In-situ NanoSIMS sulfur isotope data for pyrite are tabulated in Supplemental Table S3 and plotted in Fig. 10. In general, $\delta^{34}S$ values for hydrothermal pyrite from

Laowangzhai mine are slightly higher than those from Donggualin mine. The $\delta^{34}S$ values of As-poor pyrite zones from Donggualin mine have a range from − 6.9 (± 0.7) to 2.8 (± 0.6)‰ ($n = 21$), and the $\delta^{34}S$ values of As-rich zones are − 7.3 (± 0.6) to 2.0 (± 0.6) ‰ ($n = 15$) (Figs. 10, 11a–d). The $\delta^{34}S$ values of As-poor pyrite zones from Laowangzhai mine are − 3.6 (± 0.6) to 2.6 (± 0.6)‰ ($n = 12$), and the $\delta^{34}S$ values of As-rich zones range from − 3.6 (± 0.6) to 2.9 (± 0.6)‰ ($n = 11$; Figs. 10, 11e–f).

The sulfur isotopic compositions of framboidal pyrite from carboniferous slate are marked by extremely low $\delta^{34}S$ values ranging from − 35.0 (± 0.9) to − 25.6 (± 1.0)‰ ($n = 6$, Fig. 10). The carboniferous slate also contains several hydrothermal pyrite grains, which show a restricted range of $\delta^{34}S$ values from − 1.5 (± 0.7) to 3.9 (± 0.7)‰ (Fig. 10). These hydrothermal pyrite grains commonly enclose framboidal pyrite, with irregular boundaries between the two types (Supplemental Fig. S7a, b), suggestive of replacement of framboids by hydrothermal pyrite. The pyrite grains, located between the framboidal pyrite and hydrothermal pyrite (Supplemental Fig. S7c–f), yield $\delta^{34}S$ values ranging from − 13.4 (± 0.6) to − 9.7 (± 0.6) ‰ (Fig. 10; Supplemental Fig. S7e), midway between the $\delta^{34}S$ values of adjacent framboidal and hydrothermal pyrite (Fig. 10; Supplemental Fig. S7d, f).
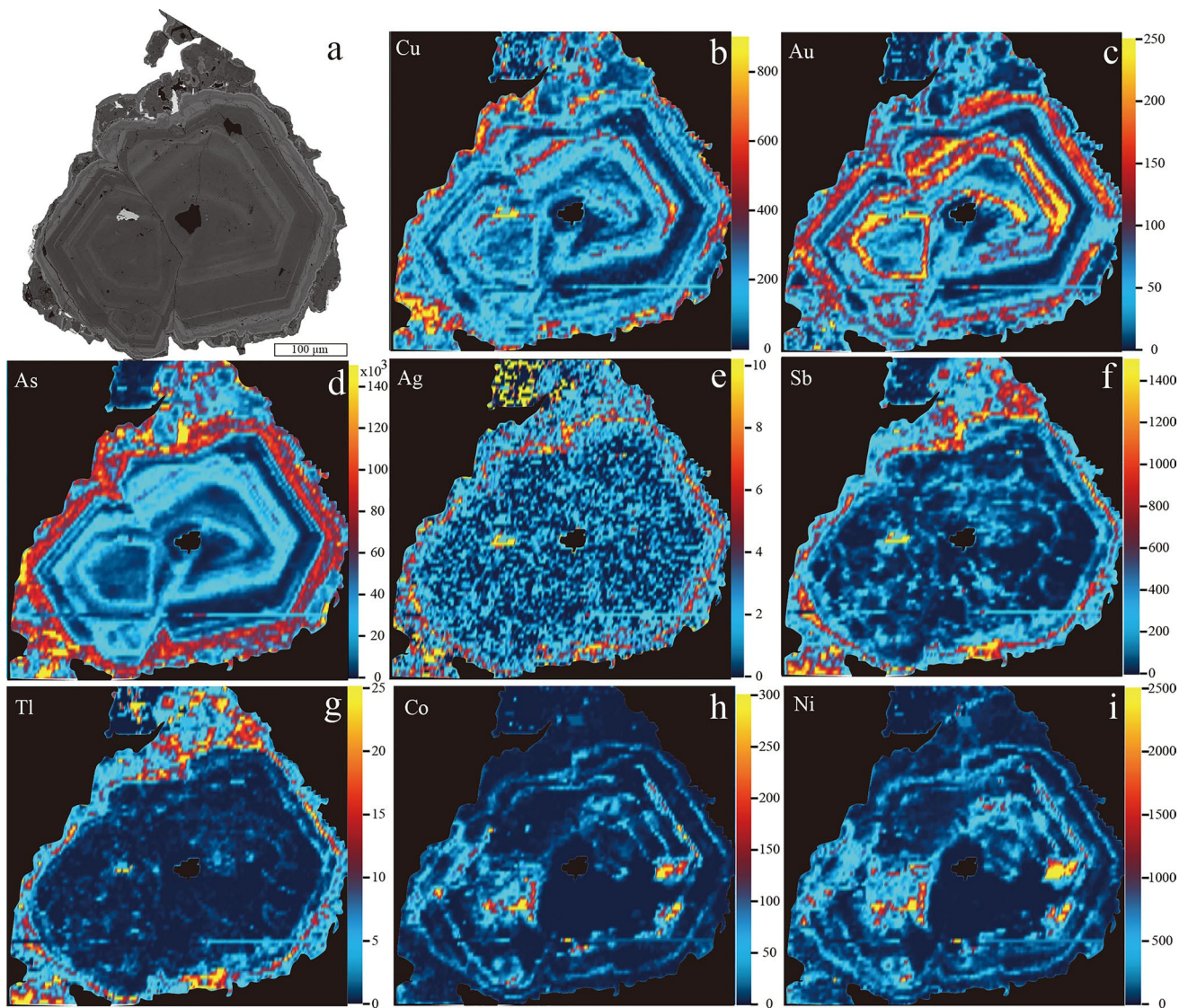
Fig. 7 LA–ICP–MS element maps of a representative pyrite grain with zoned texture from Laowangzhai mine. Scales in ppm

Discussion

Occurrence of gold

Although previous research pointed to invisible Au as the main form of Au in the Zhenyuan deposit and implied this must be in solid solution within sulfide minerals (Li et al. 2019a, b), we have observed very fine-grained (~1 μm) inclusions of native gold exclusively within As-rich pyrite (Fig. 4h). Our LA–ICP–MS mapping shows that As-rich zones also contain significant concentrations of invisible Au. In most hydrothermal gold deposits, invisible Au can be subdivided into nanoscale particles of gold-bearing minerals (most often native gold) and Au within solid solution (Cook et al. 2009; Deditius et al. 2014). As shown in Fig. 9a, concentrations of invisible Au in pyrite all plot below the

solubility saturation line for Au on a plot of Au vs. As (Reich et al. 2005). Conventionally, this was considered to infer that invisible Au occurs structurally bound rather than as nanoparticles, even if recent evidence (Ehrig et al. 2023) suggests this need not always be the case. Such a conclusion is consistent with the fact that no native gold nanoparticles were observed during TEM imaging of As-rich pyrite. EPMA data and EDS mapping suggest that As is probably incorporated into pyrite via substitution for S (Figs. 5c, 6b–d), an interpretation consistent with the conclusion that pyrite containing substituted As is formed at reduced conditions such as in orogenic gold deposits hosted by sediments (Qian et al. 2013; Stepanov et al. 2021).

A close relationship between Au and As is observed in As-bearing pyrite from many types of hydrothermal gold deposits (e.g.,Simon et al. 1999; Morey et al. 2008; Large
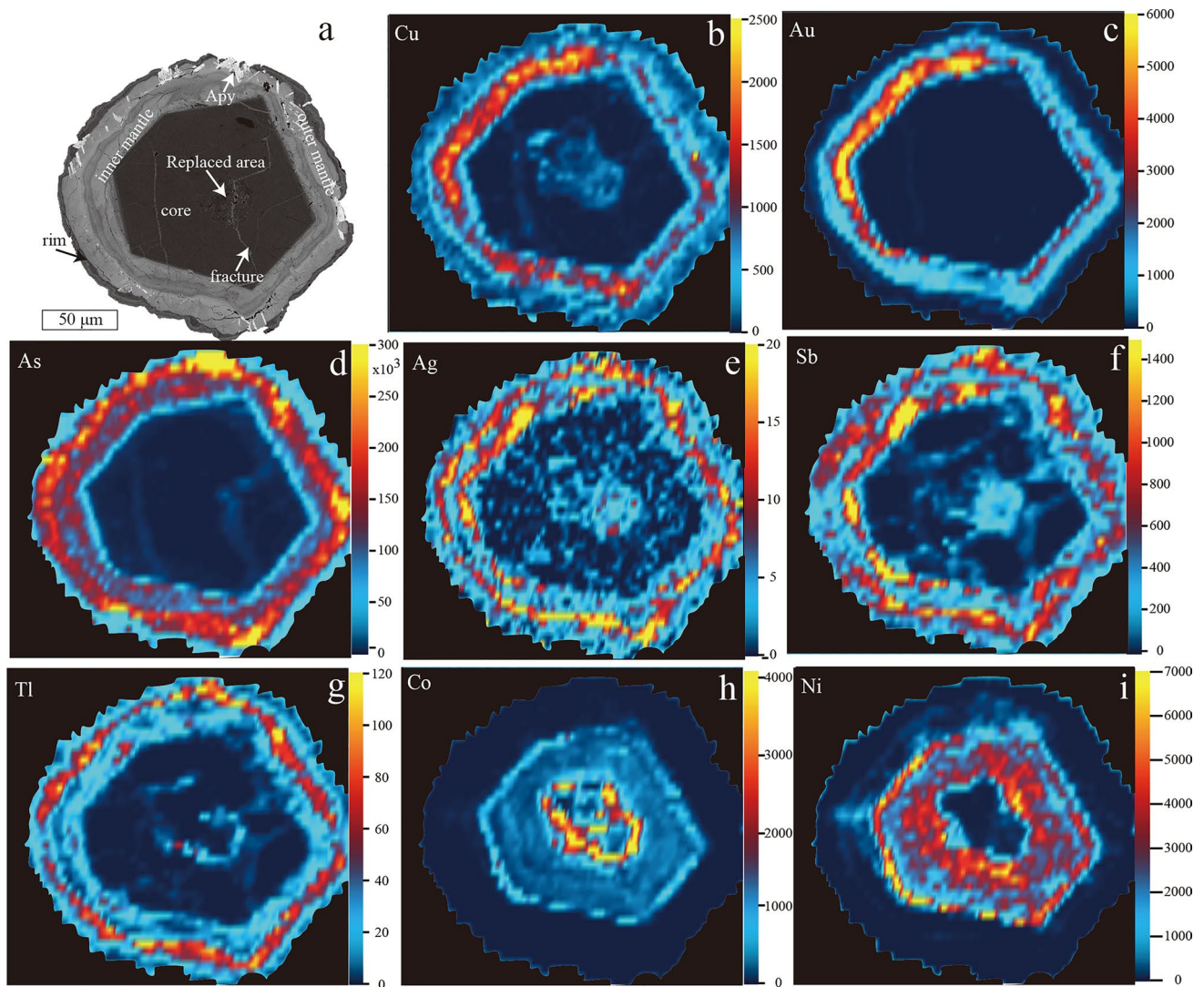
Fig. 8 LA–ICP–MS element maps of a representative pyrite grain with zoned texture from Donggualin mine. Scales in ppm

et al. 2009). Previous studies emphasized that Au was likely incorporated into As-bearing pyrite by chemisorption and electrochemical accumulation onto pyrite surfaces during crystal growth (Möller and Kersten 1994; Fleet and Mumin 1997). Kusebauch et al. (2019) proposed that enrichment in As leads to high partition coefficient for Au (adsorption and incorporation) between pyrite and fluid, thus resulting in the high Au concentrations measured in As-rich pyrite. Besides, a decrease in pyrite volume (generating porosity) during progressive enrichment of As in pyrite may also enhance Au sequestration (Xing et al. 2019). More recently, Stepanov et al. (2021) have suggested that the role of metastability in Au enrichment in the pyrite–arsenopyrite system must also be considered, and Pokrovski et al. (2021) have demonstrated how coupled Au–As redox reactions control gold incorporation in As-bearing pyrite. In the Zhenyuan gold deposit, invisible Au mainly occurs in As-rich zones,

inferring that As content in pyrite is an important influence on Au content. Considering the stable form and absence of obvious porosity in the As-rich zones, we attribute the enrichment to Au incorporation into As-enriched Fe crystallographic sites via coupled Au–As redox reactions as proposed by Pokrovski et al. (2021). We do not, however, rule out a role for surface sorption and mineral growth rate as contributors to incorporation of Au (Li et al. 2018; Wu et al. 2019).

A contribution from framboidal pyrite

Host rocks are important metal sources in many hydrothermal gold systems (e.g., orogenic gold deposits), where the ore-forming fluids are metamorphic fluids and/ or meteoric water (Powell et al. 1991; Phillips and Powell 2009). Altered mafic rocks are considered as an ideal source
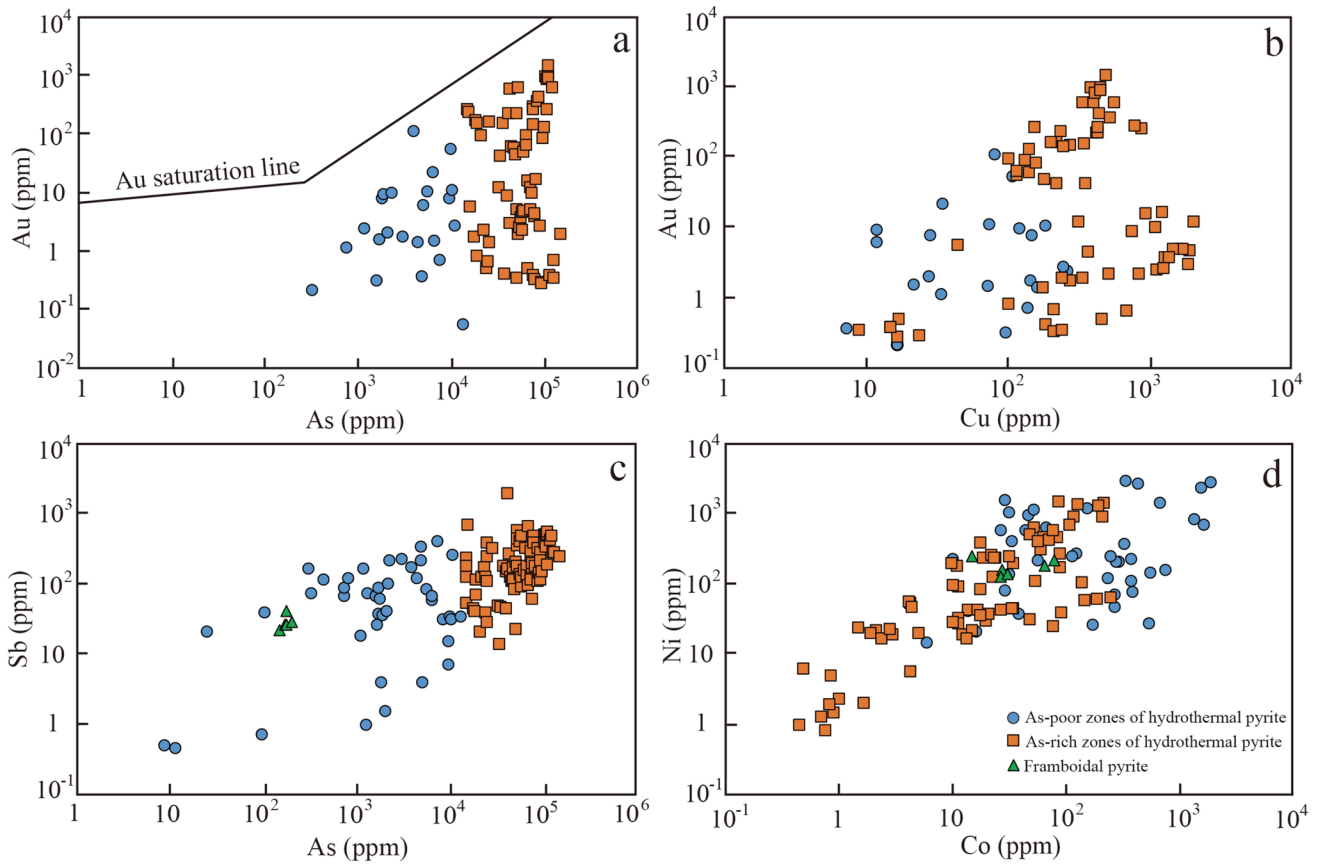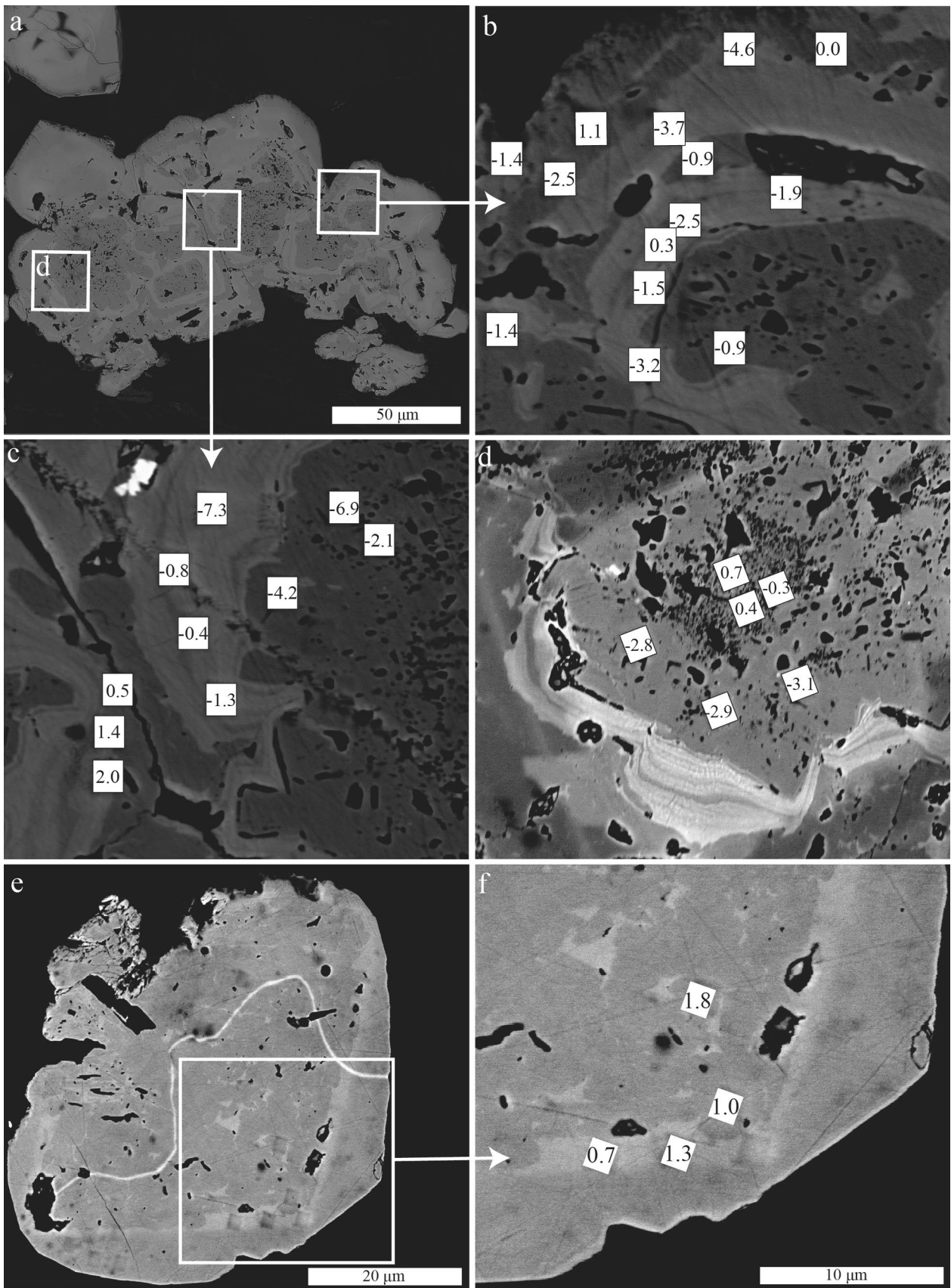
Fig. 9 Trace-element plots of framboidal pyrites and hydrothermal pyrites from Zhenyuan gold deposit. See text for additional explanation
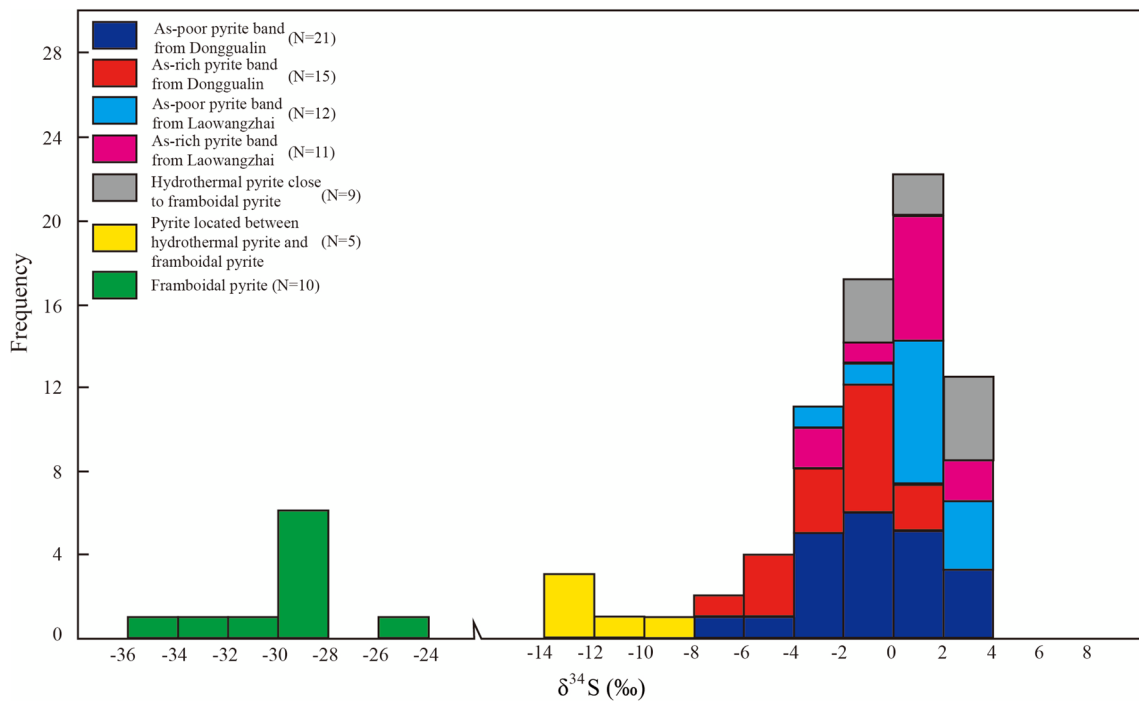
Fig. 10 Sulfur isotopic values of different types of pyrites from the Zhenyuan gold deposit

◄**Fig. 11** **a–d** Sulfur isotopic values of As-rich and As-poor zones of hydrothermal pyrite from Donggualin mine; **e, f** Sulfur isotopic values of hydrothermal pyrite from Laowangzhai mine

because of their higher Au concentrations (Bierlein and Pisarevsky 2008; Wilson et al. 2013; Pitcairn et al. 2015). Thermodynamic calculations show that carbonaceous sedimentary rocks can also generate Au-rich fluids during prograde metamorphic dehydration reactions (Tomkins 2010, 2013). Sedimentary environments are commonly favorable for formation of framboidal pyrite (Love 1971; Wilkin and Barnes 1997), resulting from a rate of crystallization that is much slower than the nucleation rate (Wilkin and Barnes 1997; Ohfuji and Rickard 2005). Prior studies have shown that bacterial sulfate reduction (BSR) could result in the framboidal pyrite having very low $\delta^{34}S$ values, approximately 40–60‰ less than contemporary seawater sulfate in an open-SO_4^{2-} ocean environment (Ohmoto and Rye 1979; Jiang and Ling 2004; Zhao et al. 2018). Published LA–ICP–MS data reveal that framboidal pyrite in carbonaceous sedimentary rocks is generally rich in Au, Ag, and other metals, and may represent a potential source for hydrothermal gold deposits (Gregory et al. 2016). Gold-rich framboidal pyrite can transform into Au-poor pyrrhotite during prograde metamorphism, releasing Au into the ore-forming fluid (Large et al. 2009, 2011; Tomkins 2010; Thomas et al. 2011). Studies of several other hydrothermal gold deposits have shown, however, that framboidal pyrite often hosts lower concentrations of Au than (later) hydrothermal pyrites and, therefore, could not have been a source for gold mineralization (Li et al. 2014; Wang and Zhu 2015), unless the framboids recrystallized after release of Au.

Since the wall rocks of framboidal pyrite (Lower Carboniferous carbonaceous slate) deposited in an open ocean setting (Zhong 1998; Deng et al. 2015). It seems the low $\delta^{34}S$ values of framboidal pyrite in Zhenyuan deposit presumably result from BSR processes in an open-SO_4^{2-} ocean environment (Ohmoto and Rye 1979; Zhao et al. 2018). The framboidal pyrite with low $\delta^{34}S$ value in Zhenyuan deposit contain very little Au concentration, but we cannot exclude a metal contribution from framboidal pyrite in rocks either distal to the deposit or present at greater crustal depths. Because the Au content of most sedimentary pyrite only has a median of 16 ppb (Gregory et al. 2015), yet sedimentary pyrite is still considered to be an important source of Au for orogenic gold deposits. Relict framboidal pyrite clearly occurs as inclusion within hydrothermal pyrite in carbonaceous slate in the Zhenyuan deposit. Framboidal pyrite is shown to be replaced by hydrothermal pyrite (Supplemental Fig. S7a, b). Furthermore, pyrite grains located between the framboidal pyrite and hydrothermal pyrite, have $\delta^{34}S$ values mid-way between those of adjacent

framboidal and hydrothermal pyrite (Fig. 10; Supplemental Fig. S7c–f), indicating that the sulfur for this type of pyrite indeed comes from a mixture of two distinct sulfur sources. These texture and sulfur isotopic data indicate that reaction between ore-forming fluid and framboidal pyrite must have occurred and framboidal pyrite, to some extent, could have contributed to the evolution of ore fluids.

Zoning in pyrite

Previous research (Peterson and Mavrogenes 2014; Wu et al. 2019; Sugiono et al. 2022) suggests that alternating As-rich and As-poor zones in pyrite can be induced by: (1) kinetic effects during crystallization including growth rate and diffusion-limited self-organization processes; (2) changes in fluid chemical composition caused by fluid–rock reactions and mixing; and (3) fault-valve controlled boiling. The rate of crystal growth indeed impacts on trace-element concentrations and the substitution of those trace elements in sulfide minerals (Barker and Cox 2011; Fougerouse et al. 2016). However, continuous crystallization with different growth rates should not result in a corrosion texture between two zones, like that observed in Zhenyuan pyrite (Fig. 4b, c, e–f). Diffusion-limited self-organization processes during crystallization were invoked to explain the sub-micron to atomic-scale zoned distribution of Au, As, and Cu (Wu et al. 2019). However, the widths of individual zones in pyrite range from a few microns to several tens of microns, and there is evidence of corrosion texture between the As-rich and As-poor zones (Fig. 4b, c, e–f). Therefore, kinetic effects during pyrite crystallization, by themselves, cannot explain formation of zoning in pyrite. However, the ultra-fine oscillatory zonation in pyrite at the micron to sub-micron scale (Fig. 5a, b) may result from local kinetics.

Several researchers (e.g.,Deditius et al. 2009; Tardani et al. 2017) have suggested that concentric micron-scale trace-element zoning in pyrite may form in response to changes in fluid chemical composition. However, changes in fluid chemical composition caused by fluid–rock reactions, sustained fluid mixing, or mineral precipitation, generally form different zones in which the compositions should vary gradually (Peterson and Mavrogenes 2014), rather than the discrete trace-element concentrations we observe in adjacent zones within the Zhenyuan samples.

As mentioned above, kinetic effects during pyrite crystallization, sustained mineral precipitation, changes in fluid chemical composition caused by fluid–rock reactions cannot result in the occurrence of alternating As-rich and As-poor zones of pyrites. The cyclic nature of the As-rich and As-poor zones, and their sharp textural and compositional boundaries is reflective of repeated and sudden variations in physico-chemical conditions, leading to the suggestion that a fault-valve cycle environment is a

likely candidate for formation of these pyrite grains (Toda et al. 2002; Peterson and Mavrogenes 2014). Fault-valve controlled boiling can trigger sharp physico-chemical changes of fluids including cooling and cause an increase in pH and fO_2 because of the loss of H_2O, H_2S, CO_2 and other volatiles to the vapor phase (Drummond and Ohmoto 1985; Williams-Jones et al. 2009). Therefore, pyrites formed under boiling and non-boiling conditions will have different textural and compositional characteristics.

The As-poor zones in the pyrite cores formed during the earliest fluid event in Zhenyuan. These As-poor zones generally preserve phosphate and silicate inclusions (Fig. 4f), and are depleted in chalcophile elements yet rich in Co and Ni (Figs. 7, 8; Supplemental Table S2). In contrast, the As-rich zones are rich in Au, Cu, Ag, Sb, and Tl but depleted in Co and Ni. High concentrations of Co and Ni in pyrite have been correlated with higher temperature in previous studies (Large and Maslennikov 2020; Liu et al. 2021), because high temperature is in favour of substitution of Fe by Co and Ni, and relatively low temperature facilitates substitution of S by As in hydrothermal pyrite (Migdisov et al. 2011; Deditius et al. 2014). Besides, Ni generally has higher solubility in fluids at higher fO_2 conditions. In contrast, Ni tends to enter pyrite at lower fO_2 conditions (Fougerouse et al. 2016; Sugiono et al. 2022). As a result, a fO_2 increase can lead to the lower Ni concentrations in pyrite. As we know boiling would trigger a temperature reduction and fO_2 increasing, the observed decreasing of Co and Ni contents from As-poor zones to As-rich zones can be interpreted by boiling (Li et al. 2022; Sugiono et al. 2022).

After formation of As-poor zones, boiling induced by subsequent episodes of faulting triggered precipitation of new As-rich zones. This was accompanied by formation of pressure shadows surrounding the pyrite crystals (Fig. 4i). Boiling can also be confirmed by published fluid inclusion studies (Zhao 2014; Li et al. 2021b) showing the coexistence of CO_2-rich fluid inclusions, CO_2–H_2O fluid inclusions, and aqueous fluid inclusions in the auriferous quartz veinlets with similar homogenization temperature. Arsenic, Au, and Cu exhibit high partitioning coefficients between liquid and vapor phase at temperatures below 300 °C (Kouzmanov and Pokrovski 2012 and references therein). Cooling and loss of water and other volatiles triggered by boiling would lead to extensive saturation of metallic elements (e.g., As, Au, and Cu) in liquid phase and consequently to higher levels of trace-element incorporation in pyrite (Velásquez et al. 2014). For instance, $As(OH)_3$ is the dominant As-bearing species in natural hydrothermal systems, over a wide range of temperature and fluid densities (Pokrovski et al. 2002; Perfetti et al. 2008). Cooling can significantly decrease As solubility and lead to precipitation of arsenopyrite and As-rich pyrite (Velásquez et al. 2014; Xing et al. 2019). Importantly, Au is primarily transported as bisulfide

complexes $(Au(HS)_2^-)$ in medium- to low-temperature, weakly acidic to neutral ore-forming systems (Seward 1973; Stefánsson and Seward 2004; Williams-Jones et al. 2009; Pokrovski et al. 2014). For native gold, a decrease of H_2S content coupled with precipitation of As-rich pyrite would drive destabilization of Au bisulfide complexes and promote Au deposition in As-rich pyrite (Zhang and Zhu 2016; Kusebauch et al. 2019; Sugiono et al. 2022). In general, the corrosion texture, abundant inclusions including arsenopyrite and stibnite, and chemical features of the As-rich pyrite zones are indicative of growth in an environment of intermittent boiling (Velásquez et al. 2014; Sugiono et al. 2022).

Potential sulfur sources

Gold is mainly transported as bisulfide complexes at conditions like those at which Zhenyuan was formed (Williams-Jones et al. 2009; Pokrovski et al. 2014). Therefore, the source of Au can be reliably constrained by investigating the source of sulfur. Pyrite is the most important Au-bearing sulfide in orogenic gold deposits, meaning that the sulfur isotope signatures of pyrite should provide direct insights into sulfur source and evolution of gold mineralization (Barker et al. 2009; Hou et al. 2016; LaFlamme et al. 2018b). Previous studies suggest that different stages of pyrite and different bands within individual zoned pyrite may have drastically variable $\delta^{34}S$ values in some hydrothermal deposits (Chen et al. 2015; Zhao et al. 2016), revealing contributions come from distinct sources or from physico-chemical changes in the ore-forming system.

Hydrothermal pyrite from quartz porphyry, lamprophyre, quartz sandstone, and carbonaceous slate ores from the Laowangzhai and Donggualin mines all display zoned textures, with alternating As-rich and As-poor pyrite zones. All have a restricted range of $\delta^{34}S$ values from − 7.3 (± 0.6) to 2.9 (± 0.6) ‰ with most data concentrated between − 4 and 4‰ (89.6%, $n = 58$) (Fig. 10; Supplemental Table S3). The abundance of sulfide minerals and absence of sulfates indicate that H_2S was the dominant form of sulfur in the ore-forming fluid. Given the temperature range (160–190 °C), low fO_2, and near-neutral pH (Ren et al. 1995; Mao et al. 2003; Liang et al. 2011), the bulk sulfur isotopic composition in ore-forming fluid at Zhenyuan should be comparable with the measured pyrite sulfur isotopic value (Ohmoto 1972). The $\delta^{34}S$ values of hydrothermal pyrites from Zhenyuan resemble those from Chang'an (− 6.2 to 7.1‰) gold deposit elsewhere in the Ailaoshan gold belt (Li et al. 2013b; Yang et al. 2021). Pyrites from the adjacent Tongchang (1.0–1.5‰) and Habo (− 1.9–2.7 ‰) porphyry Cu–Au deposits also share similar $\delta^{34}S$ values (Xu et al. 2014; Meng et al. 2016). These sulfur isotope signatures,

from deposits across the Ailaoshan district, resemble that of magmatic sulfur ($0 \pm 5‰$; Ohmoto and Rye 1979).

Commonly, sulfur from sedimentary rocks provides a much wider range of isotopic values in sulfide minerals than we report for hydrothermal pyrites from Zhenyuan (Chang et al. 2008; Chen et al. 2015; Xie et al. 2018). In addition, the rocks hosting ore were unaffected by medium- or high-grade metamorphism. Therefore, these relatively narrow range of sulfur isotopic data (most concentrated between -4 and $4‰$, 89.6%, $n = 58$) indicate that magmatic sulfur is the most plausible source for sulfur in Zhenyuan pyrite.

Apart from the $\delta^{34}S$ values, the close relationship between ore-forming age of Zhenyuan deposit and adjacent igneous rocks can also support that sulfur is derived from a magmatic source. The Oligocene epoch was interpreted as the main phase of gold mineralization at Zhenyuan based on paleomagnetic data and the Ar–Ar age of altered phlogopite (Wang et al. 2001; Deng et al. 2015; Gao et al. 2018). This age, which we infer to be that of ore formation, is in good agreement with that of the high-K alkaline and calc–alkaline magmatic rocks in the Ailaoshan tectonic belt (Liang et al. 2007; Liu et al. 2015). Moreover, published $\delta^{18}O_{H2O}$ and $\delta^{13}C_{CO2}$ data for fluid inclusions in auriferous quartz veinlets (He and Hu 1997; Liang et al. 2011) and He–Ar isotopic data from pyrite (Bi 1998) also suggest that ore-forming fluids for Zhenyuan are mainly derived from a magmatic reservoir.

Boiling can lead to an increase of fluid pH and $f\mathrm{O}_2$, resulting in the precipitation of pyrite with lower $\delta^{34}S$ values (Ohmoto 1972; Drummond and Ohmoto 1985; Palin and Xu 2000; Peterson and Mavrogenes 2014; Sugiono et al. 2022). However, the $\delta^{34}S$ values of individual As-rich pyrite zones from Donggualin mine and Laowangzhai mine (-7.3 ± 0.6 to 2.9 ± 0.6 ‰) are similar to those of the corresponding As-poor pyrite zones (-6.9 ± 0.7 to 2.8 ± 0.6 ‰; Supplemental Table S3), thus indicating that any shift in $\delta^{34}S$ values between the two zones is negligible. Small $\delta^{34}S$ shifts caused by boiling have been reported from other hydrothermal gold deposits (Velásquez et al. 2014; Li et al. 2018; Hu et al. 2020). Limited, localized boiling events are likely unable to significantly modify the bulk sulfur isotopic composition of the parent fluid (Tanner et al. 2016). Alternatively, boiling cannot cause obvious increase of fluid $f\mathrm{O}_2$, which was buffered by reaction between fluid and carbonaceous slate. Hence, the $\delta^{34}S$ values of As-rich and As-poor pyrite are similar.

Genesis of the Zhenyuan gold deposit

Large-scale igneous activity occurred in the Ailaoshan region due to post-collisional lithospheric extension involving mantle processes during the Oligocene (Liang et al. 2007; Hou and Cook 2009; Liu et al. 2015).

Magmatism strongly enhanced hydrothermal fluid activity across the region. Related magmatic–hydrothermal fluids triggered formation of porphyry Cu–Au deposits, including Tongchang and Habo, and some of these likely evolved into Au-bearing ore-forming fluids that subsequently migrated. Generally, regional fluid flow and emplacement of gold deposits are focused and controlled by regional-scale shear zones (Seltmann et al. 2011). Gold-bearing fluids migrated upward along subsidiary shear zones in the Zhenyuan region. Shearing along the Ailaoshan gold belt was initiated at 30 Ma and lasted until 22 Ma (Zhang and Schärer 1999; Cao et al. 2012; Tang et al. 2013; Liu et al. 2015), concordant with an Oligocene age of ore-formation as mentioned above.

Arsenic-poor zones in pyrite cores with high Co and Ni concentrations formed during the earliest fluid event. Arsenic, Cu, Au, Ag, Sb, and Tl were undersaturated in the fluid. With progressive strain (evidenced by the occurrence of pressure shadows; Fig. 4i), fluid pressure increased and exceeded lithostatic pressure, generating hydraulic fractures and resulting in a sudden drop of fluid pressure, triggering boiling of ore-forming fluid, at least locally (Zhao 2014; Li et al. 2021b; Fig. 12). Boiling led to oversaturation of As, Cu, Au, Ag, Sb, and Tl, and precipitation of As-rich bands, overgrowing As-poor pyrite cores. With fluid replenishment, physico-chemical conditions did not favor boiling and precipitation of As-poor pyrite bands began again overgrowing the As-rich zones. Continuous deformation induced boiling of ore-forming fluids once again. As a result, As-rich pyrite bands again overgrew the As-poor pyrite bands. Repetition of such a process produced the conspicuous rhythmic zoning described and illustrated (Fig. 12).

Conclusions and implications

Ores from the Zhenyuan deposit are altered host rocks containing disseminated pyrite and arsenopyrite, and quartz–pyrite veinlets. Pyrite in the altered host rocks and quartz–pyrite veinlets displays complex internal textures, clearly recognizable as alternating As-poor and As-rich zones. Arsenopyrite and stibnite only coexist with As-rich pyrite, whereas As-poor pyrite contains inclusions of quartz and monazite. Visible and invisible Au both only occur in the As-rich zones. LA–ICP–MS mapping and spot analysis reveal that the As-rich pyrite zones contain greater concentrations of Au, Cu, Ag, Sb, Tl, and lesser Co and Ni than the As-poor zones. *In-situ* NanoSIMS sulfur isotope analysis indicates that the $\delta^{34}S$ values of As-rich zones (-7.3 ± 0.6 to $2.9 \pm 0.6‰$) are similar to those of As-poor zones (-6.9 ± 0.7 to $2.8 \pm 0.6‰$), but nevertheless distinct from framboidal pyrite (-35.0 ± 0.9 to $-25.6 \pm 1.0‰$). Ore-forming fluids were mainly magmatic–hydrothermal
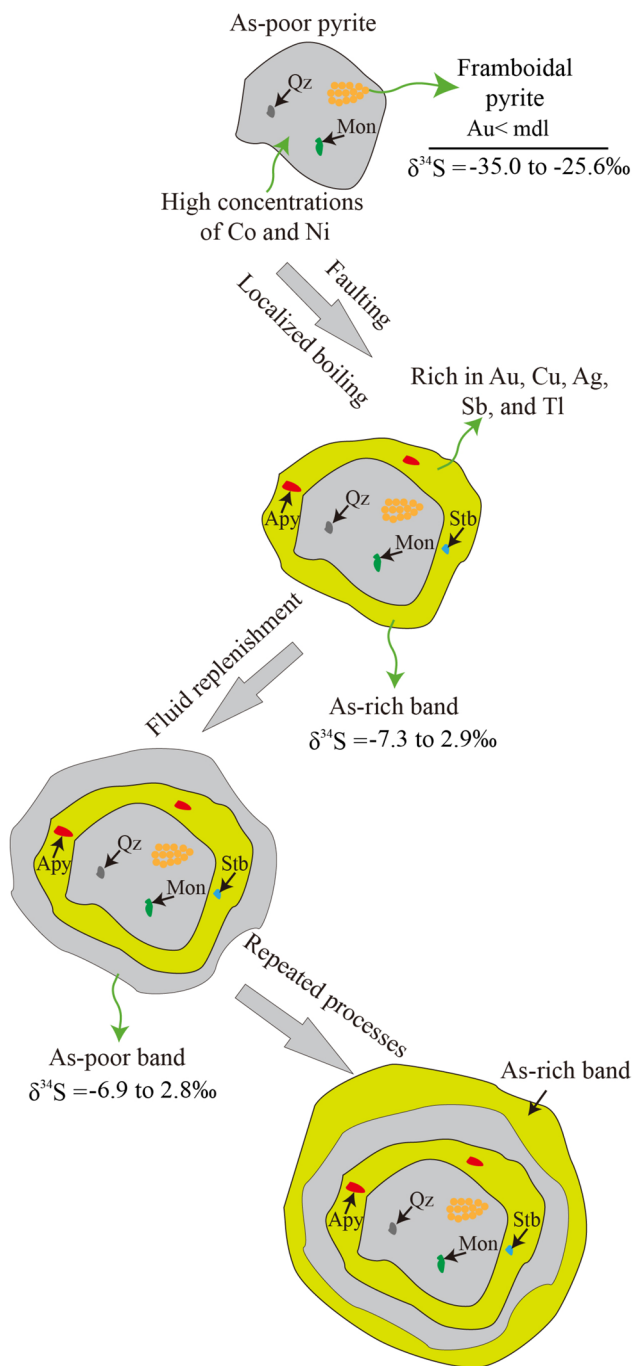
Fig. 12 Schematic showing proposed model for formation of hydrothermal pyrite with zoned texture from Zhenyuan. Mineral abbreviations: *Apy* arsenopyrite, *Mon* monazite, *Qz* quartz, *Stb* stibnite

in origin. Rhythmic As-rich and As-poor bands result from periodic opening and closing of hydraulic fractures, causing periodic boiling of the ore-forming fluid.

Pyrite is a robust mineral, capable of preserving a time-lapse sequence of successive geological events. Comparable micron-scale textures exist in analogous gold

ores elsewhere, even if perhaps not always as spectacular as those documented here. The textural information encoded in pyrite, especially when coupled with robust trace-element datasets and *in-situ* sulfur isotope signatures, can be widely utilized to provide valuable insights into the evolution of ore-forming processes.

References

Barker SL, Cox SF (2011) Oscillatory zoning and trace element incorporation in hydrothermal minerals: Insights from calcite growth experiments. Geofluids 11:48–56

Barker SL, Hickey KA, Cline JS, Dipple GM, Kilburn MR, Vaughan JR, Longo AA (2009) Uncloaking invisible gold: use of Nano-SIMS to evaluate gold, trace elements, and sulfur isotopes in pyrite from Carlin-type gold deposits. Econ Geol 104:897–904

Bi XW (1998) The metallogenetic mechanism of Ailaoshan gold belt. Bull Mineral Petrol Geochem 17:16–19

Bierlein FP, Pisarevsky S (2008) Plume-related oceanic plateaus as a potential source of gold mineralization. Econ Geol 103:425–430

Cao S, Liu J, Leiss B, Vollbrecht A, Genser J, Neubauer F, Zhao C (2012) Initiation of left-lateral deformation along the Ailao Shan-Red River shear zone: New microstructural, textural, and geochronological constraints from the Diancang Shan metamorphic massif, SW Yunnan, China. Int Geol Rev 54:348–367

Chang Z, Large RR, Maslennikov V (2008) Sulfur isotopes in sediment-hosted orogenic gold deposits: evidence for an early timing and a seawater sulfur source. Geology 36:971–974

Chen Y, Yao S, Pan Y (2014) Geochemistry of lamprophyres at the Daping gold deposit, Yunnan province, China: Constraints on the timing of gold mineralization and evidence for mantle convection in the eastern Tibetan plateau. J Asian Earth Sci 93:129–145

Chen L, Li XH, Li JW, Hofstra AH, Liu Y, Koenig AE (2015) Extreme variation of sulfur isotopic compositions in pyrite from the Qiuling sediment-hosted gold deposit, West Qinling orogen, central China: an in-situ SIMS study with implications for the source of sulfur. Miner Deposita 50:643–656

Cook NJ, Ciobanu CL, Mao J (2009) Textural control on gold distribution in As-free pyrite from the Dongping, Huangtuliang and Hougou gold deposits, North China Craton (Hebei Province, China). Chem Geol 264:101–121

Deditius AP, Utsunomiya S, Renock D, Ewing RC, Ramana CV, Becker U, Kesler SE (2008) A proposed new type of arsenian pyrite: Composition, nanostructure and geological significance. Geochim Cosmochim Acta 72:2919–2933

Deditius AP, Utsunomiya S, Ewing RC, Chryssoulis SL, Venter D, Kesler SE (2009) Decoupled geochemical behavior of As and Cu in hydrothermal systems. Geology 37:707–710

Deditius AP, Reich M, Kesler SE, Utsunomiya S, Chryssoulis SL, Walshe J, Ewing RC (2014) The coupled geochemistry of Au and As in pyrite from hydrothermal ore deposits. Geochim Cosmochim Acta 140:644–670

Deng J, Yang LQ, Ge LS, Yuan SS, Wang QF, Zhang J, Gong QJ, Wang CM (2010) Character and post-ore changes, modifications and preservation of Cenozoic alkali-rich porphyry gold metallogenic system in western Yunnan, China. Acta Petrologica Sinica 26:1633–1645

Deng J, Wang Q, Li G, Zhao Y (2015) Structural control and genesis of the Oligocene Zhenyuan orogenic gold deposit, SW China. Ore Geol Rev 65:42–54

Drummond SE, Ohmoto H (1985) Chemical evolution and mineral deposition in boiling hydrothermal systems. Econ Geol 80:126–147

Ehrig K, Ciobanu CL, Verdugo-Ihl MR, Dmitrijeva M, Cook NJ, Slattery A (2023) Lifting the cloak of invisibility: gold in pyrite from the Olympic Dam Cu-U-Au-Ag deposit. South Australia American Mineralogist 108(2):259–276

Fleet ME, Mumin AH (1997) Gold-bearing arsenian pyrite and marcasite and arsenopyrite from Carlin Trend gold deposits and laboratory synthesis. Am Miner 82:182–193

Fougerouse D, Reddy SM, Saxey DW, Rickard WD, Van Riessen A, Micklethwaite S (2016) Nanoscale gold clusters in arsenopyrite controlled by growth rate not concentration: evidence from atom probe microscopy. Am Miner 101:1916–1919

Gan T, Huang Z (2017) Platinum-group element and Re-Os geochemistry of lamprophyres in the Zhenyuan gold deposit, Yunnan Province, China: implications for petrogenesis and mantle evolution. Lithos 282:228–239

Gao L, Wang Q, Deng J, Zhang S, Yang Z (2018) Relationship Between Orogenic Gold Mineralization and Crustal Shearing Along Ailaoshan-Red River Belt, Southeastern Tibetan Plateau: new constraint from paleomagnetism. Geochem Geophys Geosyst 19:2225–2242

Ge LS, Deng J, Yang LQ, Xing JB, Yuan SS (2007) Geology and geochemistry of Daping super-large gold polymetallic deposit in Yunnan Province, China. Geology and Exploration 3:17–24

Gregory DD, Large RR, Halpin JA, Baturina EL, Lyons TW, Wu S, Danyushevsky L, Sack P, Chappaz A, Maslennikov VV, Bull SW (2015) Trace element content of sedimentary pyrite in black shales. Econ Geol 110:1389–1410

Gregory DD, Large RR, Bath AB, Steadman JA, Wu S, Danyushevsky L, Bull SW, Holden P, Ireland TR (2016) Trace element content of pyrite from the kapai slate, St. Ives Gold District, Western Australia. Econ Geol 111(6):1297–1320

Hao JL, Zhang LP, Yang W, Li ZY, Li RY, Hu S, Lin YT (2023) NanoSIMS sulfur isotopic analysis at 100 nm scale by imaging technique. Front Chem 11:1120092

He M, Hu R (1997) The deep fluid and its ore forming process of the Ailaoshan gold metallogenic belt. J Chengdu Univ Technol 24:73–77

Hou ZQ, Cook NJ (2009) Metallogenesis of the Tibetan collisional Orogen: A review and introduction to the special issue. Ore Geol Rev 36:2–24

Hou ZQ, Zaw K, Pan GT, Mo XX, Xu Q, Hu YZ, Li XZ (2007) Sanjiang Tethyan metallogenesis in SW China: Tectonic setting, metallogenic epochs and deposit types. Ore Geol Rev 31:48–87

Hou L, Peng H, Ding J, Zhang J, Zhu S, Wu S, Wu Y, Ouyang H (2016) Textures and in situ chemical and isotopic analyses of pyrite, Huijiabao Trend, Youjiang Basin, China: Implications for paragenesis and source of sulfur. Econ Geol 111:331–353

Hu HL, Fan HR, Liu X, Cai YC, Yang KF, Ma WD (2020) Two-stage gold deposition in response to H2S loss from a single fluid in the Sizhuang deposit (Jiaodong, China). Ore Geol Rev 120:103450

Jiang SY, Ling HF (2004) Stable isotope geochemistry. In: Chen J, Wang HN (eds) Geochemistry. Science Press, Beijing, pp 129–141

Keith M, Haase KM, Chivas AR, Klemd R (2022) Phase separation and fluid mixing revealed by trace element signatures in pyrite from porphyry systems. Geochim Cosmochim Acta 329:185–205

Kouzmanov K, Pokrovski GS (2012) Hydrothermal controls on metal distribution in porphyry Cu (-Mo-Au) systems. Soc Econ Geol Spec Publ 16:573–618

Kusebauch C, Gleeson SA, Oelze M (2019) Coupled partitioning of Au and As into pyrite controls formation of giant Au deposits. Sci Adv 5(5):eaav5891

LaFlamme C, Jamieson JW, Fiorentini ML, Thebaud N, Caruso S, Selvaraja V (2018a) Investigating sulfur pathways through the lithosphere by tracing mass independent fractionation of sulfur to the Lady Bountiful orogenic gold deposit, Yilgarn craton. Gondwana Res 58:27–38

LaFlamme C, Sugiono D, Thébaud N, Caruso S, Fiorentini M, Selvaraja V, Jeon H, Voute F, Martin L (2018b) Multiple sulfur isotopes monitor fluid evolution of an Archean orogenic gold deposit. Geochim Cosmochim Acta 222:436–446

Large RR, Maslennikov VV (2020) Invisible gold paragenesis and geochemistry in pyrite from orogenic and sediment-hosted gold deposits. Minerals 10:339

Large RR, Danyushevsky L, Hollit C, Maslennikov V, Meffre S, Gilbert S, Singh B, Scott R, Emsbo P, Thomas H, Singn B, Foster J (2009) Gold and trace element zonation in pyrite using a laser imaging technique: Implications for the timing of gold in orogenic and Carlin style sediment-hosted deposits. Econ Geol 104:635–668

Large RR, Bull SW, Maslennikov VV (2011) A carbonaceous sedimentary source-rock model for Carlin-type and orogenic gold deposits. Econ Geol 106:331–358

Li GJ, Wang QF, Yu L, Hu ZC, Ma N, Huang YH (2013a) Closure time of the ailaoshan paleotethys ocean: Constraints from the zircon U-Pb dating and geochemistry of the late permian granitoids. Acta Petrologica Sinica 29:3883–3900 ())

Li SH, Zhang J, Yang LQ, Wang H (2013b) Origin of metallogenic materials of the Chang'an gold deposit in the southern Ailaoshan belt: evidence from sulfur and lead isotopic composition. Geoscience 27(4):879–887

Li N, Deng J, Yang LQ, Goldfarb RJ, Zhang C, Marsh E, Lei SB, Koenig A, Lowers H (2014) Paragenesis and geochemistry of ore minerals in the epizonal gold deposits of the Yangshan gold belt, West Qinling, China. Miner Deposita 49:427–449

Li XH, Fan HR, Yang KF, Hollings P, Liu X, Hu FF, Cai YC (2018) Pyrite textures and compositions from the Zhuangzi Au deposit, southeastern North China Craton: implication for ore-forming processes. Contrib Miner Petrol 173:73

Li HJ, Wang Q, Deng J, Yang L, Dong C, Yu H (2019a) Alteration and mineralization styles of the orogenic disseminated Zhenyuan gold deposit, southeastern Tibet: Contrast with carlin gold deposit. Geosci Front 10:1849–1862

Li HJ, Wang Q, Groves DI, Deng J, Dong C, Wang X, Yang L (2019b) Alteration of Eocene lamprophyres in the Zhenyuan orogenic gold deposit, Yunnan Province, China: Composition and evolution of ore fluids. Ore Geol Rev 107:1068–1083

Li JX, Hu RZ, Zhao CH, Zhu JJ, Huang Y, Gao W, Li JW, Zhuo YZ (2020a) Sulfur isotope and trace element compositions of pyrite determined by NanoSIMS and LA-ICP-MS: new constraints on the genesis of the Shuiyindong Carlin-like gold deposit in SW China. Miner Deposita 55:1279–1298

Li HJ, Wang Q, Deng J, Yu H, Sun P, Dong C, Yang L (2020b) Source and evolution of ore fluids in the Zhenyuan orogenic gold deposit, SE Tibet: constraints from the S-C-O isotopes. Ore Geol Rev 121:103534

Li W, Cook NJ, Xie GQ, Mao JW, Ciobanu CL, Fu B (2021a) Complementary textural, trace element, and isotopic analyses of sulfides constrain ore-forming processes for the slate-hosted Yuhengtang Au deposit, South China. Econ Geol 116:1825–1848

Li Y, Wang D, Wang C, Sun Y, Pu-chi MIMA (2021b) Geology and Geochemistry of Selected Gold Deposits in the Ailaoshan Metallogenic Belt, China: Origin of Ore-Forming Fluids. Minerals 11(11):1276

Li HJ, Wang Q, Weng W, Dong C, Yang L, Wang X, Deng J (2022) Co-precipitation of gold and base metal sulfides during fluid boiling triggered by fault-valve processes in orogenic gold deposits. Ore Geol Rev 149:105090

Liang HY, Campbell IH, Allen CM, Sun WD, Yu HX, Xie YW, Zhang YQ (2007) The age of the potassic alkaline igneous rocks along the Ailao Shan-Red River shear zone: Implications for the onset age of left-lateral shearing. J Geol 115:231–242

Liang YH, Sun XM, Shi GY, Hu BM, Zhou F, Wei XH, Mo RW (2011) Ore-forming fluid geochemistry and genesis of laowangzhai large scale orogenic gold deposit in ailaoshan gold belt, Yunnan Province, China. Acta Petrologica Sinica 27:2533–2540

Liu HC, Wang YJ, Cai YF, Ma LY, Xing XW, Fan WM (2013) Zircon U-Pb geochronology and Hf isotopic composition of the Xin'anzhai granite along the Ailaoshan tectonic zone in west Yunnan Province. Geotecton Metallog 37:87–98

Liu HC, Wang YJ, Fan WM, Zi J, Cai Y, Yang G (2014) Petrogenesis and tectonic implications of Late-Triassic high εNd(t)-εHf(t) granites in the Ailaoshan tectonic zone (SW China). Sci China Earth Sci 57:181–2194

Liu J, Chen X, Wu W, Tang Y, Tran MD, Nguyen QL, Zhang ZC, Zhao Z (2015) New tectonogeochronological constraints on timing of shearing along the Ailaoshan-Red River shear zone: Implications for genesis of Ailaoshan gold mineralization. J Asian Earth Sci 103:70–86

Liu Z, Mao X, Jedemann A, Bayless RC, Deng H, Chen J, Xiao K (2021) Evolution of pyrite compositions at the Sizhuang gold deposit, Jiaodong Peninsula, Eastern China: implications for the genesis of Jiaodong-type orogenic gold mineralization. Minerals 11(4):344

Love LG (1971) Early diagenetic polyframboidal pyrite, primary and redeposited, from the Wenlockian Denbigh Grit Group, Conway, North Wales, U.K. J Sediment Petrol 41:1038–1044

Maddox LM, Bancroft GM, Scaini MJ, Lorimer JW (1998) Invisible gold: Comparison of Au deposition on pyrite and arsenopyrite. Am Miner 83:1240–1245

Mao SD, He MY, Liu F, He P (2003) Discussion on gold transportation and the ore-forming geochemical mechanism of the Laowangzhai gold field, Yunnan Province. Bull Mineral Petrol Geochem 23:228–231

Meng Z, Zhang Q, Ye L, Liu Y, Lan J, Wang D (2016) The genetic relationship between Habo alkaline intrusion and its surrounding deposits, Yunnan Province, China: geological and S-Pb isotopic evidences. Acta Geochimica 35:391–407

Migdisov AA, Zezin D, Williams-Jones AE (2011) An experimental study of Cobalt (II) complexation in Cl- and bearing hydrothermal solutions. Geochim Cosmochim Acta 75:4065–4079

Möller P, Kersten G (1994) Electrochemical accumulation of visible gold on pyrite and arsenopyrite surfaces. Miner Deposita 29:404–413

Morey AA, Tomkins AG, Bierlein FP, Weinberg RF, Davidson GJ (2008) Bimodal distribution of gold in pyrite and arsenopyrite: examples from the Archean Boorara and Bardoc shear systems, Yilgarn craton, Western Australia. Econ Geol 103:599–614

Ohfuji H, Rickard D (2005) Experimental synthesis of framboids—a review. Earth Sci Rev 71:147–170

Ohmoto H (1972) Systematics of sulfur and carbon isotopes in hydrothermal ore deposits. Econ Geol 67:551–578

Ohmoto H, Rye RO (1979) Isotopes of sulfur and carbon. In: Barnes HL (ed) Geochemistry of hydrothermal ore deposits, 2nd edn. Wiley-Interscience, New York, pp 509–567

Palenik CS, Utsunomiya S, Reich M, Kesler SE, Wang L, Ewing RC (2004) "Invisible" gold revealed: Direct imaging of gold nanoparticles in a Carlin-type deposit. Am Miner 89:1359–1366

Palin JM, Xu Y (2000) Gilt by association? Origins of pyritic gold ores in the Victory mesothermal gold deposit. Western Australia Econ Geol 95(8):1627–1634

Paton C, Hellstrom J, Paul B, Woodhead J, Hergt J (2011) Iolite: Freeware for the visualisation and processing of mass spectrometric data. J Anal at Spectrom 26:2508–2518

Perfetti E, Pokrovski GS, Ballerat-Busserolles K, Majer V, Gibert F (2008) Densities and heat capacities of aqueous arsenious and arsenic acid solutions to 350 °C and 300 bar, and revised thermodynamic properties of, and iron sulfarsenide minerals. Geochim Cosmochim Acta 72(3):713–731

Peterson EC, Mavrogenes JA (2014) Linking high-grade gold mineralization to earthquake-induced fault-valve processes in the Porgera gold deposit, Papua New Guinea. Geology 42:383–386

Phillips GN, Powell R (2009) Formation of gold deposits: Review and evaluation of the continuum model. Earth Sci Rev 94:1–21

Pitcairn IK, Craw D, Teagle DA (2015) Metabasalts as sources of metals in orogenic gold deposits. Miner Deposita 50:373–390

Pokrovski GS, Kara S, Roux J (2002) Stability and solubility of arsenopyrite, FeAsS, in crustal fluids. Geochim Cosmochim Acta 66:2361–2378

Pokrovski GS, Akinfiev NN, Borisova AY, Zotov AV, Kouzmanov K (2014) Gold speciation and transport in geological fluids: Insights from experiments and physicalchemical modelling. Geol Soc London Spec Pub 402:9–70

Pokrovski GS, Escoda C, Blanchard M, Testemale D, Hazemann JLF, Gouy S, Kokh MA, Boiron MC, de Parseval F, Aigouy T, Menjot L, de Parseval P, Proux O, Rovezzi M, Béziat D, Salvi S, Kouzmanov K, Bartsch T, Pöttgen R, Doet T (2021) An arsenic-driven pump for invisible gold in hydrothermal systems. Geochem Perspect Lett 17:39–44

Powell R, Will TM, Phillips GN (1991) Metamorphism in Archaean greenstone belts: Calculated fluid compositions and implications for gold mineralization. J Metamorph Geol 9:141–150

Qi XX, Wang XH, Zhu LH, Hu ZC, Li ZQ (2010) Validation on age of Neoproterozoic intrusions from northeastern margin of Indochina block, western Yunnan and its tectonic implication: Evidence from zircon LA-ICP-MS U-Pb dating and geochemistry. Acta Petrologica Sinica 26:2141–2154

Qian G, Brugger J, Testemale D, Skinner W, Pring A (2013) Formation of As(II)-pyrite during experimental replacement of magnetite under hydrothermal conditions. Geochim Cosmochim Acta 100:1–10

Reich M, Kesler SE, Utsunomiya S, Palenik CS, Chryssoulis SL, Ewing RC (2005) Solubility of gold in arsenian pyrite. Geochim Cosmochim Acta 69:2781–2796

Reich M, Deditius A, Chryssoulis S, Li JW, Ma CQ, Parada MA, Barra F, Mittermayr F (2013) Pyrite as a record of hydrothermal fluid

evolution in a porphyry copper system: a SIMS/EMPA trace element study. Geochim Cosmochim Acta 104:42–62

Ren SL, Qin GJ, Chi SC, Tang SH (1995) Au origin of Laowangzhai-Donggualin gold deposit, Zhenyuan County, Yunnan Province. J China Univ Geosci 20:47–52

Román N, Reich M, Leisen M, Morata D, Barra F, Deditius AP (2019) Geochemical and micro-textural fingerprints of boiling in pyrite. Geochim Cosmochim Acta 246:60–85

Seltmann R, Konopelko D, Biske G, Divaev F, Sergeev S (2011) Hercynian post-collisional magmatism in the context of Paleozoic magmatic evolution of the Tien Shan orogenic belt. J Asian Earth Sci 42(5):821–838

Seward TM (1973) Thio complexes of gold and the transport of gold in hydrothermal ore solutions. Geochim Cosmochim Acta 37:379–399

Shi G, Sun X, Pan W, Hu B, Qu W, Du A, Li C (2012) Re-Os dating of auriferous pyrite from the Zhenyuan super-large gold deposit in Ailaoshan gold belt, Yunnan Province, southwestern China. Chin Sci Bull 57:4578–4586

Simon G, Huang H, Penner-Hahn JE, Kesler SE, Kao L (1999) Oxidation state of gold and arsenic in gold-bearing arsenian pyrite. Am Miner 84:1071–1079

Stefánsson A, Seward TM (2004) Gold (I) complexing in aqueous sulphide solutions to 500°C at 500 bar. Geochim Cosmochim Acta 68:4121–4143

Stepanov AS, Large RR, Kiseeva ES, Danyushevsky LV, Goemann K, Meffre S, Zhukova I, Belousov IA (2021) Phase relations of arsenian pyrite and arsenopyrite. Ore Geol Rev 136:104285

Sugiono D, LaFlamme C, Thébaud N, Martin L, Savard D, Fiorentini M (2022) Fault-induced gold saturation of a single auriferous fluid is a key process for orogenic gold deposit formation. Econ Geol 117(6):1405–1414

Sun XM, Zhang Y, Xiong DX, Sun WD, Shi G, Zhai Y, Wang SW (2009) Crust and mantle contributions to gold-forming process at the Daping deposit, Ailaoshan gold belt, Yunnan, China. Ore Geol Rev 36:235–249

Tang Y, Liu J, Tran MD, Song Z, Wu W, Zhang Z, Zhao Z, Chen W (2013) Timing of left-lateral shearing along the Ailaoshan-Red River shear zone: Constraints from zircon U-Pb ages from granitic rocks in the shear zone along the Ailaoshan Range, Western Yunnan, China. Int J Earth Sci 102:605–626

Tang X, Gu LX, Li QL, Du ZM, Yang SH, Feng LJ, Li JH (2023) An apparatus for plasma cleaning and storage of transmission electron microscopy specimens and specimen holders. Microsc Res Tech 86(2):198–207

Tanner D, Henley RW, Mavrogenes JA, Holden P (2016) Sulfur isotope and trace element systematics of zoned pyrite crystals from the El Indio Au-Cu-Ag deposit. Chile Contrib Mineral Petrol 171:33

Tardani D, Reich M, Deditius AP, Chryssoulis S, Sánchez-Alfaro P, Wrage J, Roberts MP (2017) Copper-arsenic decoupling in an active geothermal system: A link between pyrite and fluid composition. Geochim Cosmochim Acta 204:179–204

Thomas HV, Large RR, Bull SW, Maslennikov V, Berry RF, Fraser R, Froud S, Moye R (2011) Pyrite and pyrrhotite textures and composition in sediments, laminated quartz veins, and reefs at Bendigo Gold Mine, Australia: Insights for ore genesis. Econ Geol 106:1–31

Toda S, Stein RS, Sagiya T (2002) Evidence from the AD 2000 Izu islands earthquake swarm that stressing rate governs seismicity. Nature 419:58–61

Tomkins AG (2010) Windows of metamorphic sulfur liberation in the crust: Implications for gold deposit genesis. Geochim Cosmochim Acta 74:3246–3259

Tomkins AG (2013) On the source of orogenic gold. Geology 41:1255–1256

Velásquez G, Béziat D, Salvi S, Siebenaller L, Borisova AY, Pokrovski GS, De Parseval P (2014) Formation and deformation of pyrite and implications for gold mineralization in the El Callao District. Venezuela Econ Geol 109(2):457–486

Wang L, Zhu Y (2015) Multi-stage pyrite and hydrothermal mineral assemblage of the Hatu gold district (west Junggar, Xinjiang, NW China): Implications for metallogenic evolution. Ore Geol Rev 69:243–267

Wang JH, Qi L, Yin A, Xie GH (2001) Emplacement age and PGE geochemistry of lamprophyres in the Laowangzhai gold deposit, Yunnan, SW China. Sci China Earth Sci 44:146–154

Wang ZH, Guo XD, Ge LS, Wang L, Chang CJ, Cong RX, Zhang HY (2012) Geochemical characteristics of monzonite granite from the Daping gold mining area, Yunnan Province and geological significance. Geol Explor 48(3):618–628

Wang C, Bagas L, Lu Y, Santosh M, Du B, McCuaig TC (2016) Terrane boundary and spatio-temporal distribution of ore deposits in the Sanjiang Tethyan Orogen: Insights from zircon Hf-isotopic mapping. Earth Sci Rev 156:39–65

Wang Y, Zhang H, Zhang H, Chai P, Hou Z (2020) Gold in the lithosphere of the western South China Block, SW China: Insights from quartz porphyries from the giant Zhenyuan gold deposit. Ore Geol Rev 119:103312

Wang Q, Yang L, Zhao H, Groves DI, Weng W, Xue S, Li HJ, Dong CY, Yang LQ, Li DP, Deng J (2022) Towards a universal model for orogenic gold systems: a perspective based on Chinese examples with geodynamic, temporal, and deposit-scale structural and geochemical diversity. Earth Sci Rev 224:103861

Wilkin RT, Barnes HL (1997) Formation process of framboidal pyrite. Geochim Cosmochim Acta 61:323–339

Williams-Jones AE, Bowell RJ, Migdisov AA (2009) Gold in solution. Elements 5:281–287

Wilson SA, Ridley WI, Koenig AE (2002) Development of sulfide calibration standards for the laser ablation inductively-coupled plasma mass spectrometry technique. J Anal at Spectrom 17:406–409

Wilson CJL, Schaubs P, Leader LD (2013) Mineral precipitation in the quartz reefs of the Bendigo gold deposit, Victoria, Australia. Econ Geol 108:259–278

Wu YF, Fougerouse D, Evans K, Reddy SM, Saxey DW, Guagliardo P, Li JW (2019) Gold, arsenic, and copper zoning in pyrite: A record of fluid chemistry and growth kinetics. Geology 47:641–644

Xiao WJ, Ao SJ, Yang L, Han CM, Wan B, Zhang JE, Zhang ZY, Li R, Chen ZY, Song SH (2017) Anatomy of composition and nature of plate convergence: Insights for alternative thoughts for terminal India-Eurasia collision. Sci China Earth Sci 60:1015–1039

Xie Z, Xia Y, Cline JS, Pribil MJ, Koenig A, Tan Q, Yan J (2018) Magmatic origin for sediment-hosted Au deposits, Guizhou province, China: In situ chemistry and sulfur isotope composition of pyrites, Shuiyindong and Jinfeng deposits. Econ Geol 113:1627–1652

Xing Y, Brugger J, Tomkins A, Shvarov Y (2019) Arsenic evolution as a tool for understanding formation of pyritic gold ores. Geology 47:335–338

Xu L, Bi X, Hu R, Tang Y, Jiang G, Qi Y (2014) Origin of the ore-forming fluids of the Tongchang porphyry Cu-Mo deposit in the Jinshajiang-Red River alkaline igneous belt, SW China: Constraints from He, Ar and S isotopes. J Asian Earth Sci 79:884–894

Xu B, Hou ZQ, Griffin WL, Zheng YC, Wang T, Guo Z, Hou J, Santosh M, O'Reilly SY (2021) Cenozoic lithospheric architecture and metallogenesis in Southeastern Tibet. Earth Sci Rev 214:103472

Yang LQ, Liu JT, Zhang C, Wang QF, Ge LS, Wang ZL, Zhang J, Gong QJ (2010) Superimposed orogenesis and metallogenesis:

An example from the orogenic gold deposits in Ailaoshan gold belt, Southwest China. Acta Petrologica Sinica 26:1723–1739

Yang L, Wang Q, Large RR, Mukherjee I, Deng J, Li H, Yu H, Wang X (2021) Fluid source and metal precipitation mechanism of sediment-hosted Chang'an orogenic gold deposit, SW China: Constraints from sulfide texture, trace element, S, Pb, and He-Ar isotopes and calcite C-O isotopes. Am Miner 106:410–429

Zhang HR, Hou ZQ (2015) Pattern and process of continent-continent collision orogeny: A case study of the Tethys collisional Orogen. Acta Geol Sin 89:1539–1559

Zhang LS, Schärer U (1999) Age and origin of magmatism along the Cenozoic Red River shear belt, China. Contrib Miner Petrol 134:67–85

Zhang HC, Zhu YF (2016) Geology and geochemistry of the Huilvshan gold deposit, Xinjiang, China: Implications for mechanism of gold precipitation. Ore Geol Rev 79:218–240

Zhang HC, Zhu YF (2017) Genesis of the Mandongshan gold deposit (Xinjiang, NW China): T-P-fS_2 and phase equilibria constraints from the Au-As-Fe-S system. Ore Geol Rev 83:135–151

Zhang Y, Sun XM, Shi GY, Xiong DX, Zhai W, Pan WJ, Hu BM (2011) SHRIMP U-Pb dating of zircons from diorite batholith hosting Daping gold deposit in Ailaoshan gold deposit, Yunnan Province, China. Acta Petrologica Sinica 27:2600–2608

Zhang C, Yang LQ, Zhao K, Liu JT, Li P (2012) Structure controlling pattern of the Laowangzhai gold deposit, Ailaoshan orogenic belt, western Yunnan, China. Acta Petrologica Sinica 28:4109–4124

Zhang J, Deng J, Chen HY, Yang LQ, Cooke D, Danyushevsky L, Gong QJ (2014a) LA-ICP-MS trace element analysis of pyrite from the Chang'an gold deposit, Sanjiang region, China: Implication for ore-forming process. Gondwana Res 26:557–575

Zhang JC, Lin YT, Yang W, Shen WJ, Hao JL, Hua S, Cao MJ (2014b) Improved precision and spatial resolution of sulfur isotope analysis using NanoSIMS. J Anal at Spectrom 29:1934–1943

Zhang HC, Zhu YF, Salvi S, Wu YF, Gilbert S (2022) Complex fluid source of the multistage pyrite-bearing Huilvshan gold deposit (west Junggar, NW China): Insight from pyrite texture, sulfur isotope and trace element compositions. Ore Geol Rev 149:105081

Zhao J, Liang JL, Ni SJ, Xiang QR (2016) In-situ sulfur isotopic composition analysis of Au-bearing pyrites by using Nano-SIMS in Yangshan gold deposit. Gansu Province Mineral Depos 35(4):653–662

Zhao J, Liang J, Long X, Li J, Xiang Q, Zhang J, Hao J (2018) Genesis and evolution of framboidal pyrite and its implications for the ore-forming process of Carlin-style gold deposits, southwestern China. Ore Geol Rev 102:426–436

Zhao K (2014) Geochemistry of Ore-Forming Processes in the Ailaoshan Orogenic Gold Belt, Yunnan. Dissertation, China University of Geosciences, Beijing

Zheng J, Shen P, Feng W (2022) Hydrothermal apatite record of ore-forming processes in the Hatu orogenic gold deposit, West Junggar, Northwest China. Contrib Miner Petrol 177:27

Zhong DL (1998) The paleo-Tethyan orogenic belts, western Yunnan and Sichuan provinces. Science Press, Beijing